Atmospheric characterization of directly imaged exoplanets with JWST /MIRI

Camilla Danielski, Jean-Loup Baudino, Pierre-Olivier Lagage, Anthony Boccaletti, Rene Gastaud, Alain Coulais, Bruno Bézard

Draft version October 3, 2018
Typeset using LaTeX **modern** style in AASTeX61

ATMOSPHERIC CHARACTERIZATION OF DIRECTLY IMAGED EXOPLANETS WITH JWST/MIRI.

Camilla Danielski,[1,2,3] Jean-Loup Baudino,[4] Pierre-Olivier Lagage,[1] Anthony Boccaletti,[5] René Gastaud,[1] Alain Coulais,[6,1] and Bruno Bézard[5]

[1] *AIM, CEA, CNRS, Université Paris-Saclay, Université Paris Diderot, Sorbonne Paris Cité, F-91191 Gif-sur-Yvette, France*

[2] *GEPI, Observatoire de Paris, PSL Université, CNRS, 5 Place Jules Janssen, 92190 Meudon, France*

[3] *Institut d'Astrophysique de Paris, CNRS, UMR 7095, Sorbonne Université, 98 bis bd Arago, 75014 Paris, France*

[4] *Department of Physics, University of Oxford, Oxford, UK*

[5] *LESIA, Observatoire de Paris, Université PSL, CNRS, Sorbonne Université, Univ. Paris Diderot, Sorbonne Paris Cité, 5 place Jules Janssen, F-92195 Meudon, France*

[6] *LERMA, Observatoire de Paris, CNRS, F-75014, Paris, France*

Submitted to AJ

Abstract

The Mid-Infrared instrument (MIRI) on board the *James Webb Space Telescope* will perform the first ever characterization of young giant exoplanets observed by direct imaging in the 5-28 μm spectral range. This wavelength range is key for both determining the bolometric luminosity of the cool known exoplanets and for accessing the strongest ammonia bands. In conjunction with shorter wavelength observations, MIRI will enable a more accurate characterization of the exoplanetary atmospheric properties.

Here we consider a subsample of the currently known exoplanets detected by direct imaging and we discuss their detectability with MIRI, either using the coronagraphic or the spectroscopic modes. By using the Exo-REM atmosphere model we calculate the mid-infrared emission spectra of fourteen exoplanets, and we simulate MIRI coronagraphic or spectroscopic observations. Specifically we analyze four coronagraphic observational setups, which depend on (i) the target-star and reference-star offset (0, 3, 14 mas), (ii) the wave-front-error (130, 204 nm rms), (iii) the telescope jitter amplitude (1.6, 7 mas). We then determine the signal-to-noise and integration time

Corresponding author: Camilla Danielski
camilla.danielski@cea.fr

values for the coronagraphic targets whose planet-to-star contrasts range from 3.9 to 10.1 mag.
We conclude that all the MIRI targets should be observable with different degrees of difficulty, which depends on the final in-flight instrument performances.

Furthermore, we test for detection of ammonia in the atmosphere of the coolest targets. Finally, we present the case of HR 8799 b to discuss what MIRI observations can bring to the knowledge of a planetary atmosphere, either alone or in combination with shorter wavelength observations.

Keywords: techniques: high angular resolution, imaging spectroscopy / planets and satellites: atmospheres, fundamental parameters, gaseous planets/ instrumentation: high angular resolution, spectrographs, telescopes, MIRI, JWST

1. INTRODUCTION

In the field of study of exoplanets, high-contrast imaging enables us to probe the outermost part of an exo-planetary system. Due to observational biases, the exoplanets detected so far by direct imaging are young objects (< 100 Myr), orbiting at large distances ($d_P \geq 10$ AU) nearby stars ($d_\star \leq 100$ pc). Given that they reside in the outskirts of the planetary systems, the stellar irradiation they receive is negligible, causing their temperature to decrease in time. Consequently, they need to be young to be bright enough for being detected.

These young planets produce radiation from the heat of formation and gravitational contraction and they are therefore brighter at infrared wavelengths than their older equivalents. This particular aspect makes them optimal targets for spectroscopic studies with direct imaging from which it is possible to derive important information about the planetary architecture, the atmospheric structure and dynamics, and about planetary formation.

In recent years new extreme adaptive optic cameras mounted on 8-m class telescopes, like the VLT/Spectro-Polarimetric High-contrast Exoplanet REsearch (SPHERE, Beuzit et al. 2008) or the Gemini Planet Imager (GPI, Macintosh et al. 2014), have enabled infrared detection and characterization of exoplanets at very small angular separation from their host stars, reaching contrasts as large as $5 \cdot 10^{-7}$ at $0.5''$ (Vigan et al. 2015; Mesa et al. 2017). This new generation of instruments enables spectroscopic observations, which are needed to characterize the atmosphere of the exoplanets (such as their atmospheric structure, dynamics, and molecular content). However, the limited spectral window in which they operate ($\Delta\lambda = 1$ - 2.3 μm) is a serious shortcoming to study this kind of exoplanets, especially the coolest ones. Only planets warmer than 1200 K have a large enough thermal emission in this wavelength range. Cooler planets like, for instance, HD 95086 b ($T_{\rm eff} \sim 1050$ K), present a very low flux in the Y-band ($\Delta\lambda = 0.96$ - 1.08 μm), J-band ($\Delta\lambda = 1.11$ - 1.33 μm) and H-band ($\Delta\lambda = 1.48$ - 1.78 μm), making the detection difficult (e.g. Chauvin et al. 2018). Though, at longer wavelengths, like the L′-band ($\Delta\lambda = 3.49$ - 4.11 μm) where the planetary flux is higher, the detection is clear (e.g. Rameau et al. 2013b).

In addition, observations restricted to the 1 - 2.3 μm spectral range do not allow to sample the strongest features of molecules like CH_4 ($\sim$3.3 μm), CO_2 ($\sim$ 4.3 μm), PH_3 ($\sim$ 4-5 μm), CO ($\sim$5 μm), NH_3 ($\sim$10.65 μm), C_2H_2 and HCN (both $\sim$ 14 μm, visible only in a case of planets with a C/O ratio larger than 1).

The situation will dramatically change with the launch of the *James Webb Space Telescope* (JWST) in mid-2020.

Among JWST instruments, the Mid-Infrared Instrument (MIRI, Rieke et al. 2015; Wright et al. 2015 and references therein) will be pivotal to the characterization of gas-giant exoplanets. MIRI will overcome the limited sensitivity of the largest ground-based observatories (e.g. the Large Binocular Telescope Interferometer, Hinz 2009) extending planetary characterization to the mid-infrared thermal regime, where

objects are too faint to be detected from the ground. MIRI covers a wavelength range from 5-28 μm and it combines imaging (Bouchet et al. 2015), coronagraphy (Boccaletti et al. 2015), low resolution spectroscopy (LRS, Kendrew et al. 2015) and medium resolution spectroscopy with integral-field unit (Wells et al. 2015); additional information about MIRI can be found at https://jwst-docs.stsci.edu/display/JTI/Mid-Infrared+Instrument%2C+MIRI.

In this manuscript we will mostly focus on simulated exoplanet observations with the coronagraphic and low resolution spectrometer observational modes.

MIRI coronagraphic imaging incorporates one Lyot mask (30″x 30″) at λ = 23 μm and three four-quadrant phase masks (4QPM) at λ = 10.65, 11.40, 15.50 μm, which cover a field of view of 24″x 24″(Rouan et al. 2000). The 4QPM transparent masks confer phase differences in diverse parts of the focal plane and make the light interfering more destructively than with a normal Lyot mask. This concept allows to reach an inner working angle (IWA, separation at which the throughput of an off-axis object achieves 50%) of $\sim \lambda/D$. It is the first time that such coronagraphs are used in a space-based instrument.

Among its various capabilities MIRI coronagraphic mode was specifically conceived to detect the ammonia feature (located at λ = 10.65 μm) and measure its intensity (Boccaletti et al. 2015). The first 4QPM filter is centered on the ammonia absorption band, while the second one is strategically placed beside the first one to give the level of the continuum. Coronagraphic observations, in combination with shorter wavelength observations, will also allow us to better constrain the planetary parameters (such as the effective temperature, bolometric luminosity, chemical equilibrium or non-equilibrium chemistry and gravity). In such a way, MIRI will support comprehensive modeling of the atmospheric properties of an exoplanet (e.g. Bonnefoy et al. 2013).

In this manuscript we present the exoplanetary science that can be done with the 4QPM coronagraph and low-resolution spectrometer observational modes. For the coronagraphic mode, in particular, we present the degree of difficulty of various sources' observations, according to possible observational conditions and on-orbit performance.

In § 2 we discuss the selection of targets studied in this manuscript and how we have chosen the type of observation, i.e. coronagraphic versus spectroscopic. In § 3 we introduce the Exo-REM planetary models and PHOENIX stellar models used for our analysis. § 4.1 presents our MIRI coronagraphic mode simulations. In § 5 we elaborate on the results, discussing both sources' detectability via coronagraphic or spectroscopic observations, and the significance of ammonia detection in the atmosphere of the "cold" planets belonging our target list. We discuss in § 5.4 the science constraints that MIRI can put when working in synergy with NIR observatories and we present our conclusions in § 6.

Table 1. Coronagraphic modes of MIRI

Filter	Coronagraph	Mean filter transmission [%]	Stop transmission [%]	λ_C [μm]	Bandwidth$^*_{(50\%)}$ [μm]	IWA [arcsec]	Rejection† [on-axis]
F1065C	4QPM1	72	62	10.575	0.558	0.33	304
F1140C	4QPM2	78	62	11.30	0.537	0.36	293
F1550C	4QPM3	68	62	15.50	0.731	0.49	334
F2300C	Lyot spot	71	72	22.75	4.504	2.16	918

*Width at half maximum filter transmission while Boccaletti et al. (2015) is quoting the width at 10% of the maximum.

†Values are marginally different from Boccaletti et al. (2015) due to different simulations parameters.

2. TARGETS

For our study we selected from the Extrasolar Planets Encyclopaedia[1] a subsample of known directly imaged exoplanets with a planetary mass $M_P < 13$ M$_J$, effective temperature $T_P \leq 2000$ K, and located at angular distance d $> \lambda_C/D$ as well as $d < 10''$ from the host star, where λ_C is the central wavelength of each coronagraphic filter (see Tab. 1) and where D is the telescope mirror diameter. Table 2 summarizes the list of the selected targets with their mean parameters. For each target we also indicated which MIRI mode we used to simulate the observations: coronagraphic (C) or spectroscopic (S). The choice between the type of observations depends on the contrast and the angular distance between the exoplanet and its host star. To make the selection we have used the JWST simulated Point Spread Function (PSF) simulation tool at 11.30 μm i.e. the WebbPSF[2] software to determine the PSF as a function of the angular distance from the star itself. Fig. 1 shows that for four exoplanets (i.e. VHS 1256-1257 b, HD 106906 b, 2M2236+4751 b and ROXs 42B b) the contrasts (which is measured using the Exo-REM model, see §3) and angular distances are such that coronagraphic observations are not required. The stellar PSF contribution to the signal is indeed much lower than the planet contribution at the angular distance of the planet.

For two exoplanets (i.e. 2M1207 b and GJ 504 b), the stellar contribution at the planet location is comparable to the planet signal itself, hence coronagraphic observations, as well as spectroscopic observations, can be considered. For all the sources whose contrast is well below the stellar PSF signal, coronagraphic observations are really beneficial in terms of signal-to-noise ratio.

[1] http://exoplanet.eu

[2] https://jwst.stsci.edu/science-planning/proposal-planning-toolbox/psf-simulation-tool-webbpsf

Table 2. Table of analyzed targets. For each target we report here the planetary effective temperature (T_P), the planetary radius (R_P), surface gravity (log(g)), angular separation (sep), stellar-to-planet contrast for non equilibrium models, filter F1550C ($C^{neq}_{\rm FC3}$), the stellar 2MASS K_s magnitude (K_s), the stellar effective temperature ($T_{\rm eff}$), the system distance (d) and the type of observations analyzed (OBS: C for coronograph, S for spectroscopy).

Name	T_P [K]	R_P [$R_{\rm J}$]	log(g) [cgs]	sep [$''$]	$C^{neq}_{\rm FC3}$[mag]	K_s	$T_{\rm eff}$[K]	d [pc]	OBS
2M1207 b	1000	1.5	4	0.78	3.88^{w}	11.945	2500	52.4	C, S
2M2236+4751 b	1050^{m}	$1^{\dagger}$	$4.5^{\dagger}$	3.7	6.87	9.148	$4000^{\dagger}$	63	S
51 Eri b	700	1.	3.5	0.45	10.07	4.537	7400	29.4	C
β Pictoris b	1700	1.65	3	0.42	7.23	$3.48^{\ddagger}$	8000	19.3	C
GJ 504 b	544	0.96	3.9	2.48^{m}	8.83	4.033	6234	17.56	C, S
HD 106906 b	1950	$1^{\dagger}$	$4^{\dagger}$	7.11	7.15	6.683	6516	92	S
HD 95086 b	1050^{m}	1.3	3.3	0.6	9.58	6.789	7550	90.4	C
HIP 65426 b	1300	1.5	4.5	0.83	8.09	6.771	8840	111.4	C
HR 8799 b	950	0.96	4.8	1.7241	8.19	5.24	7430	39.4	C
HR 8799 c	1150	1.07	5.4	0.9481	7.71	-	-	-	C
HR 8799 d	1150	1.14	5.4	0.6587	7.88	-	-	-	C
HR 8799 e	1200	1.06	5.2	0.3855	8.19	-	-	-	C
ROXs 42B b	1975	2.5	3.6	1.5	2.02	8.671	2200	135	C, S
VHS 1256-1257 b	880	$1^{\dagger}$	4.24	8.06	3.49	10.044	2620	12.7	S

References— 2M1207 b: Chauvin et al. (2004) ; 2M2236+4751 b: Bowler et al. (2017) 51 Eri b: Macintosh et al. (2015); β Pictoris b: Lagrange et al. (2009); GJ 504 b: Kuzuhara et al. (2013); HD 106906 b: Bailey et al. (2014); HD 95086 b: Rameau et al. (2013a); HIP 65426 b: Chauvin et al. (2017); HR8799 b,c,d,e: Marois et al. (2008, 2010), ROXs 42B b: Currie et al. (2014); VHS 1256-1257 b : Gauza et al. (2015);

($\dagger$) assumed;
($\ddagger$) magnitude in K band.;
(m) mean value of a given range;
(w) WISE W3 ($\lambda \sim 12\mu$m, Wright et al. 2010) contrast;
Note that HR 8799 system's parameters are retrieved from the fit on the available data, non-equilibrium case, see § 3.

Concerning GJ 504 we decided to keep the companion GJ 504 b among our targets despite the uncertainty on the age estimation of its host star GJ 504 (Fuhrmann and Chini 2015, D'Orazi et al. 2017) which could classify the companion as a brown-dwarf with mass $M \approx 30$ - 40 $M_{\rm J}$. The decision was driven by the fact that the planetary very low temperature, which allows for ammonia studies, and large angular separation, make it a good test case for MIRI coronagraphy observations. Furthermore, the planet is very much documented by ground-based observations and it provides an interesting comparison (Bonnefoy et al., submitted).

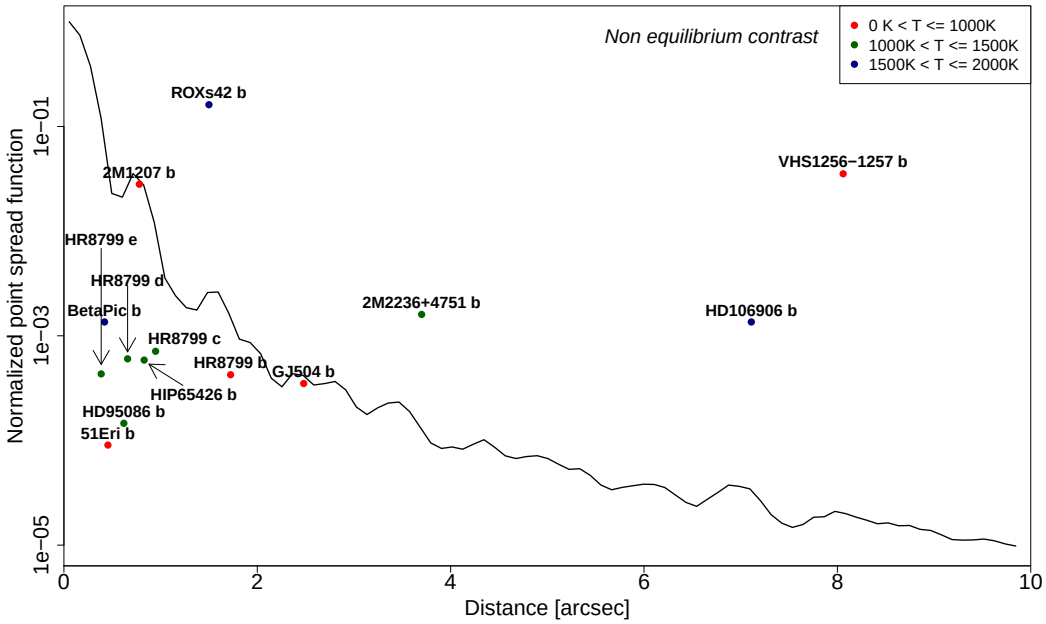

Figure 1. Non coronagraphic point spread function versus the distance to the peak signal, normalized to 1. The 1D curve has been measured from a simulated image of a MIRI observation with a filter at 11.3μm (using the WebbPSF software). The signal has been averaged over an annulus of 1 pixel width (i.e. 0.11″). Dots indicate the planet-to-star contrast of the targets under consideration. Colors correspond to the temperature of the target as indicated in the top legend. Those planetary systems whose planet-to-star contrast lies above the curve will be observed with the spectroscopic mode. Note that 2M1207 b contrast takes into account the host star and disk flux.

Similarly, the mass of VHS 1256-1257 b is contentious due to a controversy about the distance of the system itself. In the discovery paper (Gauza et al. 2015) the authors report a parallactic distance of d = 12.7 ± 1.0 pc, while a more recent study (Stone et al. 2016) reports a spectrophotometric distance of d = 17.2 ± 2.6 pc. A farther system would imply the mass of the planetary companion to be $M \approx 35$ M_J, locating it in the brown dwarfs class.

3. MODELS

To compute the synthetic spectra of planets we have used the Exoplanet Radiative-convective Equilibrium Model (Exo-REM), developed by Baudino et al. 2015, 2017 and tailored for directly imaged exoplanets. For each target, the parameters required to generate a model (effective planetary temperature T_P, surface gravity log(g), radius R_P and distance d to Earth) were taken from the literature.
A different approach has been used for HR 8799 system. Given its scientific interest we produced for each companion the best set of models (one at the equilibrium and one at non-equilibrium) fitting the available near-infrared observations (see §3).

For the stellar spectrum models we used the BHAC15 PHOENIX spectra (Baraffe et al. 2015).

Table 3. Physical parameters of the planetary companions in the HR 8799 system where the best fit (i.e. minimal χ^2, non-equilibrium model) was performed on data by Bonnefoy et al. (2016), within 2 σ. Best fit parameters with equilibrium chemistry (k_{zz}= 0) are also shown in the bottom panel. All cases are with clouds and solar metallicity. Uncertainties for the equilibrium chemistry are not reported as no agreement with the data was found within 2 σ.

	T_P [K]	log(g) [cgs]	k_{zz} [$cm^2 s^{-1}$
HR 8799 b	950^{+100}_{-0}	$4.8^{+0.1}_{-0.1}$	10^8
HR 8799 c	1150^{+50}_{-0}	$5.4^{+0}_{-0.8}$	10^8
HR 8799 d	1150^{+50}_{-150}	$5.4^{+0}_{-0.6}$	10^8
HR 8799 e	1200^{+0}_{-300}	$5.2^{+0.2}_{-1.4}$	10^8
HR 8799 b, c, e	1200	5.2	0
HR 8799 d	1200	5.4	0

HR 8799 PLANETARY MODELS

We performed a χ^2 analysis (following the one performed in Baudino et al. 2015), comparing four grids of models to the observational data of the HR 8799 system from Bonnefoy et al. (2016). Each grid corresponds to a combination of set of clouds and a type of atmospheric chemistry. More precisely we considered a case with silicate and iron clouds (with a mean particle radius of 30 μm and $\tau_{\rm ref}$ = 0.5) and a case with no clouds at all. For the atmospheric chemistry we considered both equilibrium and non-equilibrium chemistry with an eddy mixing coefficient k_{zz} = 10^8 cm^2 s^{-1}. Refer to Baudino et al. 2017 for a description of the non-equilibrium chemistry formalism. Grids were generated with Exo-REM spanning a temperature T_P range from 400 K to 1200 K (by step of 50 K), a surface gravity $\log_{10}(g)$ range from 3.0 to 5.4 (by step of 0.2, where g is in cgs units) and a metallicity (z) range from -0.2 dex to +1.4 dex (by step of 0.1).

Tab. 3 shows the parameters of the best fit on the data (Bonnefoy et al. 2016) for each planet in the HR 8799 system. The best model is always for solar metallicity (z=0), with clouds, non-equilibrium chemistry and at less than 2 σ from the observations (less than1 σ for HR 8799 e). We also kept the best cases with equilibrium chemistry for comparison purposes, though we note that all cases deviate from the observations at more than 2 σ. Figure 2 shows the corresponding spectra.

Note that, since the publication by Bonnefoy et al. (2016), the Exo-REM model has been updated (see Appendix B by Baudino et al. 2017) and the grids used in the present paper are different from the ones used in the original analysis. The result of the characterization is hence slightly different.

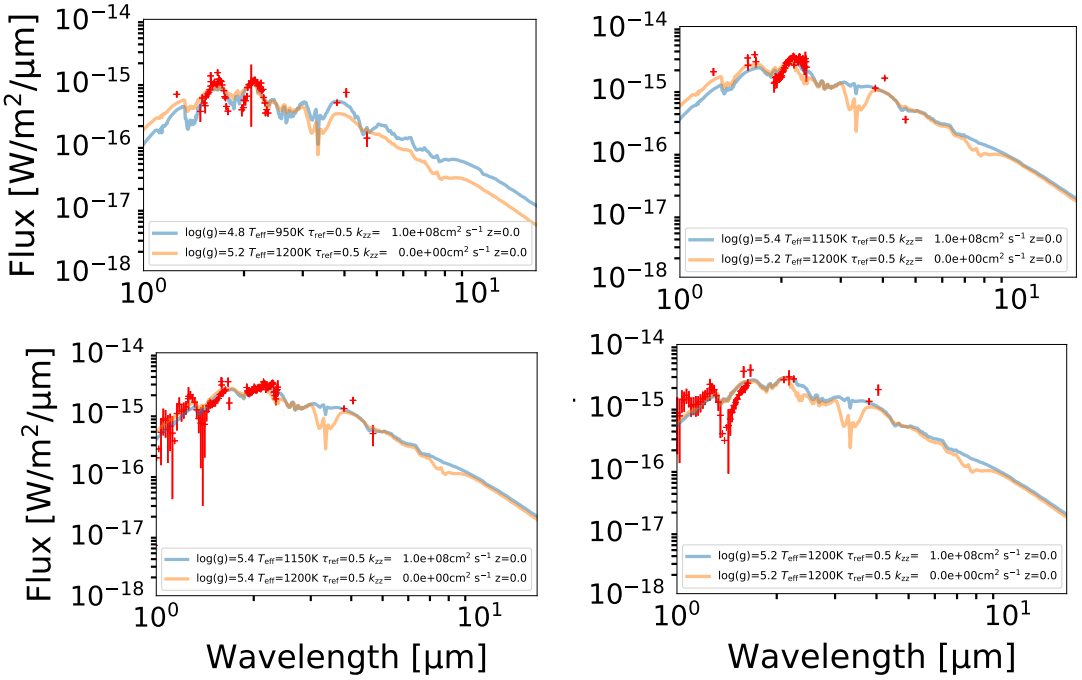

Figure 2. Exo-REM synthetic spectra (equilibrium *orange* and non-equilibrium *light-blue*) with the best χ^2 compared to HR 8799 system observations (*red*, Bonnefoy et al. 2016. From top left, clockwise: HR 8799 b, HR 8799 c, HR 8799 e, HR 8799 d.

4. CORONAGRAPHIC SIMULATIONS

4.1. *Coronagraphic observations simulations*

In this section, we will focus on describing the coronagraphic observations simulation process; for a thorough description of both MIRI coronagraphs and target acquisition process refer to Boccaletti et al. 2015.

The simulation of a science image is a two-step process that consists in simulating the diffraction patterns of all objects in the system under study (on-axis pattern for the star as well as off axis patterns for planets, see § 4.1.1) and in creating the science image itself, which also includes sources of noise (see § 4.1.2). This procedure is applied to both the observed planetary system and a reference star (hereafter called "reference" for simplicity). Note that, for contrast maximization reasons, the acquisition of a reference image is necessary because it will be subtracted from the science target image. For a best result, the magnitude and spectrum of the reference should be identical to the ones of the target star.

4.1.1. *Coronagraphic PSFs and coronagraphic image simulation*

To build the diffraction patterns we followed the principle of operation of the 4QPM coronagraph (Fig.1 by Boccaletti et al. 2015). Note that, in order to encompass different observational settings, we considered five specific cases k to account for variations of the wavefront error (WFE), for different amplitudes of the telescope jitter and for different offsets between the target star and the reference star. Table 4

Table 4. The different cases analyzed and their respective instrumental configuration for the observations. The value of (x,y) position of star and reference are relative to the center of the coronagraphic mask.

Case	WFE rms [nm]	Jitter amplitude [mas]	Star (x, y) [mas]	Reference (x, y) [mas]	Star-Reference Offset [mas]
k_A	130	1.6	0 ; 0	0 ; 0	0
k_B	130	1.6	0 ; 0	+2.12 ; +2.12	3
k_C	204	7	0 ; 0	+2.12 ; +2.12	3
k_D	204	7	-4.95 ; -4.95	+4.95 ; +4.95	14
k_P	204	0	0 ; 0	0 ; 0	0

NOTE—For case k_P (photon noise) no jitter and no stellar offset have been included and its WFE = 204 nm has been chosen for conservative reasons. The only difference from the other cases is within the PSFs generation step, the science image generation is the same as the other cases (see § 4.1.1 and § 4.1.2 for more details).

shows the configuration for these cases: an optimistic one (k_A), a pessimistic one (k_D) and two intermediate cases (k_B and k_C). Each case represents a different configuration of the following values: for the wave front error we used WFE ∼130 nm and WFE ∼204 nm root mean square (rms) (also used in Boccaletti et al. 2015), while for the amplitude of the jitter ($jamp$) of the pointing we used a minimum value of 1.6 mas (E. Nalan, private communication, July 8, 2015) and a maximum value of 7 mas (1 σ dispersion value).

We modeled the telescope jitter by changing the pointing step by step for a discrete number of iterations. As currently not enough information is available to foresee the jitter performances in space, we set the number of iterations to be what we thought to be a realistic number i.e. N = 1000. Figure 3 compares the intensity of the normalized stellar residuals (i.e. after subtracting the normalized reference's coronagraphic image from the target's normalized coronagraphic image) for the number of jitter steps N = 10, 100, 1000 for k_A and filter F1065C. The highest the number of jitter steps, the faintest the speckle residuals. More specifically, the telescope jitter was applied on both X and Y axes and each jitter step followed the normal distribution $\sim \mathcal{N}(0, jamp^2)$ where $jamp$ = 1.6 mas or 7 mas, depending on the case k we are in. For each of the thousand frames we supposed the telescope to be steady, hence no smearing effect was included during the integration. The effect of this approximation (i.e. no smearing) is negligible when averaging over a thousand frames. We note that a jitter amplitude $jamp$ = 1.6 mas corresponds to a spatial movement on the detector of 1.45 $\cdot 10^{-2}$ pixel, while for a $jamp$ = 7 mas the movement corresponds to 6.3 $\cdot 10^{-2}$ pixel[3].

[3] An offset in the focal plane corresponds to a shift of phase in the coronagraphic pupil, meaning that, even if the jitter amplitude is small, it has an impact on the final image due to the high sensitivity of the phase-mask coronagraph to phase changes.

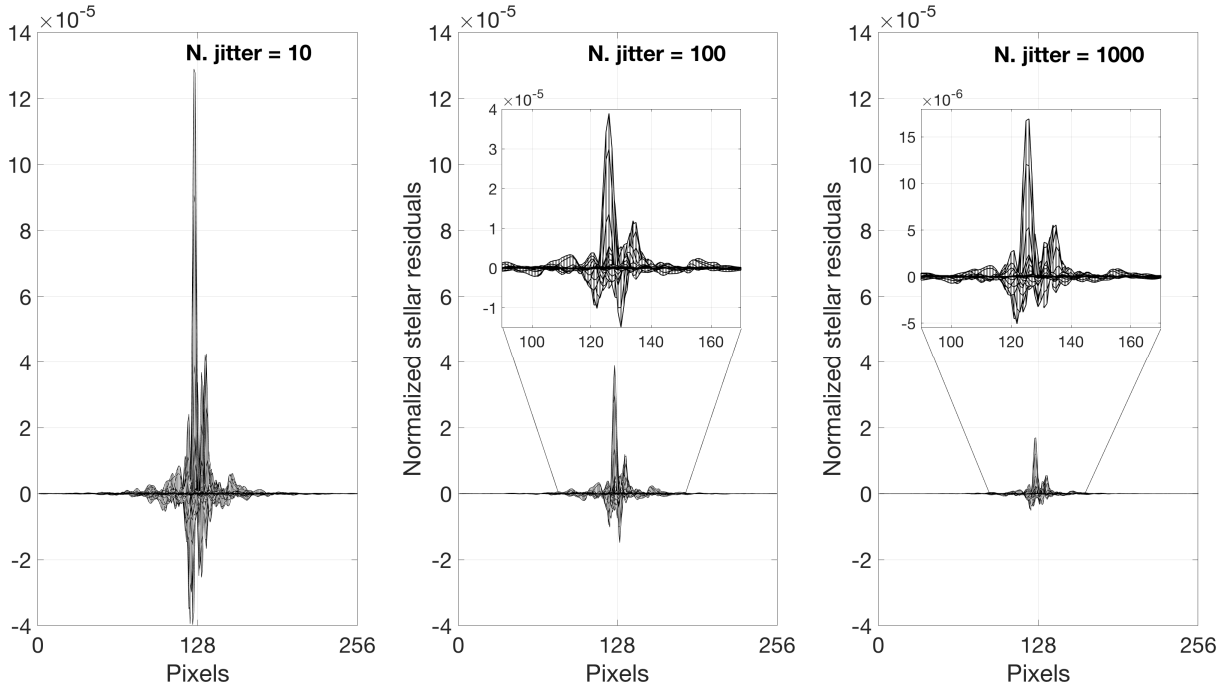

Figure 3. F1065C k_A normalized coronagraphic residuals (i.e. given by the star - reference coronagraphic images subtraction) in a case of 10 (*left*), 100 (*center*) and 1000 (*right*). For the central and right panel zoom-in of the speckles are shown to better appreciate the structure and intensity values. The images show a vertical cut on the intensity of the speckles, where the X axis represents the pixels in the X direction of the image. Units corresponds to the number of pixels as seen in the X axis of Fig. 7; pixel 128 is the central pixel. Telescope jitter was applied in both X and Y axis, with a jitter amplitude $jamp$ = 1.6 mas (see §4.1.1 for more details on the jitter simulations).

Jitter realizations were applied differently for target star and reference, meaning that their coronagraphic PSFs differ. Accordingly, when no telescope jitter is included and when target star and reference star have the same offset (e.g. in case k_P), both stellar coronographic PSFs are identical. Concerning the offset between the target star and the reference, we considered one offset of 0 mas, one of 3 mas where the star is perfectly centered behind the coronagraph, and one of 14 mas where both stars are displaced in opposite direction on the coronagraph center, each one at a distance of 1σ jitter amplitude value from the center.

The fifth case (k_P) represents an ideal case where no jitter and no star-reference offset were added and where, for conservative reasons, we used WFE $\sim$ 204 nm rms.

To choose the best position angle (PA) for the science image simulations, we studied the effect of the coronagraphic transmission as a function of the MIRI PA[4], hereinafter referred to as "PA" for simplicity.

To map the coronagraphic transmission we produced a set of coronographic images (with no jitter) within $\pm 4''$ from the center of the coronagraphic mask. For each

[4] The MIRI position angle has an offset angle from the JWST V3 axis of 4.45°.

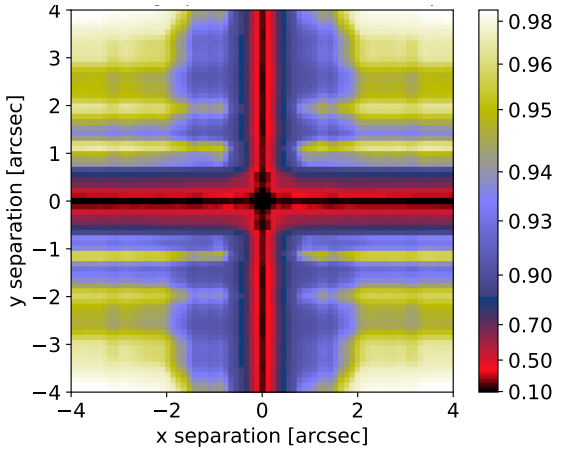

Figure 4. Coronagraphic F1550C transmission map within ±4″ from the center of coronagraph mask.

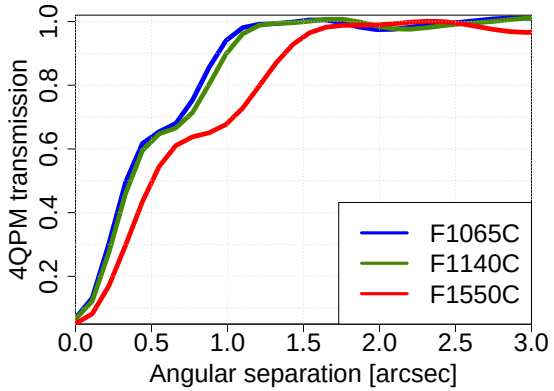

Figure 5. Radial transmission of the MIRI 4QPM coronagraph filters. Transmission is measured as a function of the distance from the center of the 4QPM mask, at 45°, where pixel size is 0.11″x 0.11″.

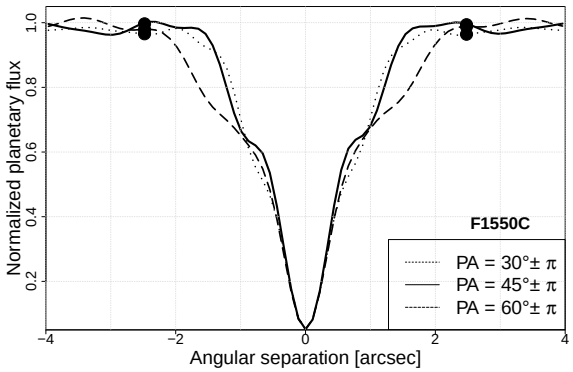

(a) Normalized flux as a function of the angular separation between the planet and the star, for an exoplanet located at PA = 30°, 45°, 60°. Values in the X-axis reports the angular distance relative to the center of the coronagraphic mask along these specific PAs. Black full dots on the positive X-axis side correspond to the dots at PA = 30°, 45°, 60° of Fig. 6b, while those on the negative side to those at PA = 210°, 225°, 240° (Fig. 6b).

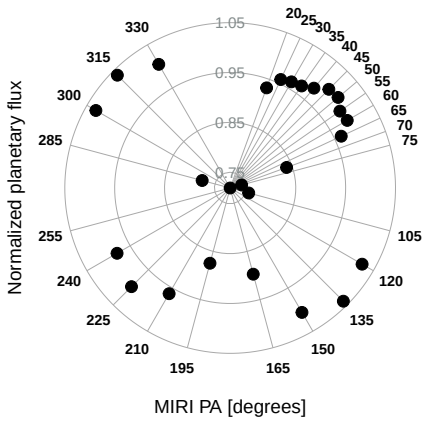

(b) Normalized flux as a function of the PA, measured for a fixed angular separation (sep = 2.48″). Each black full dot shows the planetary flux value measured for a planet when located at the position angle labeled in the outermost ring. Radial scale corresponds to the flux values marked on each gray circle.

Figure 6. Normalized planetary flux as a function of the angular separation (*left*) and the MIRI position angle PA (*right*) for filter F1550C (IWA ∼ 0.49″). Flux at 315° and 135° is larger than those at 45° or 225° mainly because of the stellar pupil shift applied (see Tab. 5). For some PA the normalized flux is larger than 1 (but within 3% deviation) because the PSF used for the normalization was itself produced at 45°(see §4.1.1), and hence presenting a lower flux than at 315°, asymmetry due to the stellar shift mentioned above.

image, generated using a different combination of planetary *sep* (-4″ – 4″) and PA (0° - 360°), we measured the total flux. This process was performed for the three 4QPM filters. We show in Figure 4 the coronagraphic transmission map measured for filter F1550C. We note that the coronagraphic transmission, as a function of the position of the source, scales with wavelength. For instance the radial transmission at wavelength 15.5 micron, is the radial attenuation at 10.65 expanded by multiplying the separation angle by 15.5/10.65. We show in Figure 5 the transmission at PA = 45° for the three 4QPM filters.

Figure 6a shows how the total flux in filter F1550C varies as a function of the angular separation (for a fixed PA), while Figure 6b shows how the total flux varies depending on the PA (for a fixed *sep*).

Consequently, in order to account for the minimal coronagraphic attenuation, we suggest to set the planetary companions along the diagonals of the detector, i.e., PA = 45°, 135°, 225°, 315°. For our simulations we set the PA of all planetary companions at PA = 45°. The only exception is the HR 8799 system, which needed a different configuration in order to simultaneously image all four planets, without having any of them hidden by the coronagraph axes (i.e. where the coronographic attenuation is maximal and the centroid measurement error is the largest; Lajoie et al. 2014). We did not vary the choice of PA over the filters to be coherent in our results.

After having set the planetary PA we generated for each 4QPM filter (Tab. 1), for each element in the coronagraph target list (Tab. 2) and for each case (Tab. 4), one coronagraphic image for the star, one coronagraphic image for the reference, and one coronographic image for each planet in the system. Finally, for each planetary system we produced a total of 15 sets (i.e. 3 filters, 5 cases) of 3 coronagraphic images (i.e. the trio star, planet, reference).

These images (an example is given in Fig. 7) were normalized to the PSF of the

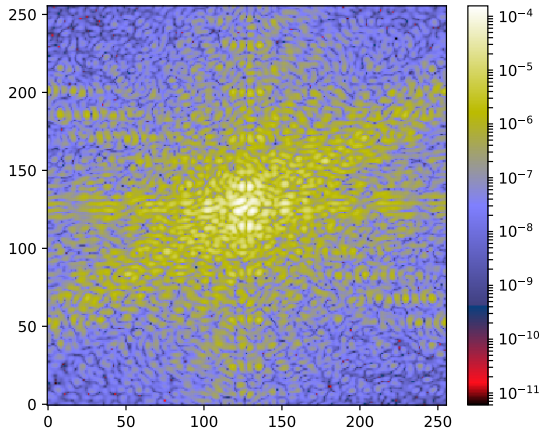

Figure 7. Coronagraphic image of the target star (F1065C, k_A, N jitter = 1000) normalized to the PSF of the target star as seen on the imager at 45°, far from the center so that the coronagraphic effect is negligible. The color scale indicates the contrast with respect to the image maximum.

Table 5. Values of MIRI and telescope parameters utilized in the simulations.

System parameters	values
Mirror diameter	6.57 m
Primary mirror area	25 m^2
Amplitude of telescope defocus	2 mm
Telescope transmission	0.9216
MIRI transmission	0.9272
Pupil rotation*	0.5°
Star pupil shift*	3%
Reference pupil shift**	0%
Read out noise amplitude	14 e^-
Detector quantum efficiency	$\geq$ 60%
Detector subarray dimension	256 x 256 pxl
Pixel field of view	0.11″x 0.11″
Flat field error measurement	1e-3
Detector saturation	250000 e^-
Limit K_s magnitude for coronagraph saturation	$\sim$ -1.9

NOTE— (*) relative to the telescope pupil; (**) relative to the star pupil
.

target star as seen on the imager at 45°, far from the center so that the coronagraphic effect is negligible.

4.1.2. *Science image creation*

To produce the science image we multiply the normalized coronagraphic image of each object by its respective spectrum, integrated over the MIRI bands (see § 3 for more details on the modelling). Note that the spectral flux in the coronagraphic image, and consequently its photon noise, is a function of the planetary system distance, the telescope mirror area, both telescope and optics transmissions, the MIRI detector quantum efficiency, and of the integration time $t_{\rm int}$. Table 5 summarizes the values of these and more parameters, specific of both MIRI and the telescope, that were used during the simulations.

From the resulting three images (star, reference and planet) we merged stellar target and planetary image by adding them together. In the case of a system with multiple planets, we produce one image for each planet and we combined them together with the target star image.

Thereafter we added to both planetary system (star + planet) and reference images both sky and telescope background (Glasse et al. 2015, Fig.1) and photon noise. At

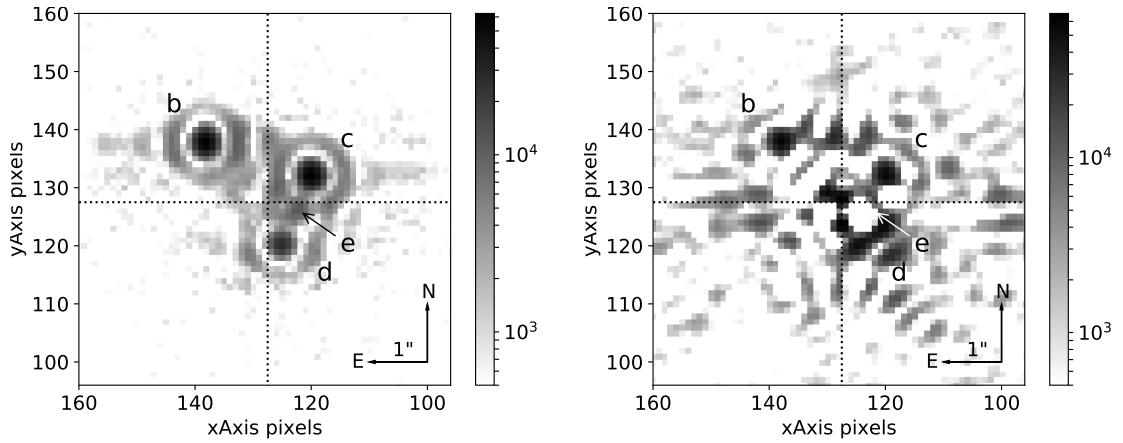

Figure 8. Zoom-in of the HR 8799 system final scientific image (k_A, *left* and k_D, *right*, equilibrium case, filter F1065C, $t_{\rm int}$ = 1800 s) after the reference image subtraction. The color scale unit is electrons, pixel size is 0.11″

the detector level we added readout noise (Ressler et al. 2015) and flat field error measurement (Tab. 5). Note that, for k_P, the only sources of noise are Poisson noise, background, and detector noise.

Finally we obtained the science image by subtracting the reference image from the planetary system image. Figure 8 shows the science image of the HR 8799 system, for cases k_A and k_D, both at F1065C, in the atmospheric equilibrium case.
We remark that, throughout the whole science image simulation process, both star and reference images share the same WFE, telescope defocus amplitude, and telescope jitter amplitude (but not the same jitter realizations, which differ for the two objects). Variations in the WFE rms and/or in the jitter amplitude values between star and reference images are not taken into account in this study.

4.2. *Coronagraphic SNR and photometric uncertainties*

To account for different noise realizations, and to estimate the photometric uncertainties, we generated for each target, filter, case ($k_{\rm A,B,C,D,P}$) and for different integration times, a cube of n = 500 scientific images (see § 4.1.2). Images within a cube were produced using the same set of three normalized coronagraphic images: one for the target star, one for the planet and one for the reference star (see 4.1.1), meaning that science images in the cube differ only in random noise but not in WFE and telescope jitter.
We then performed aperture photometry on each image to measure the planetary flux F by using a mask of fixed aperture centered on the planet's centroid, which was measured by knowing the exact position of the planet on the FOV. The radius of the photometric mask used was r = 2.5 pixels for filters F1065C and F1140C, and r = 3.5 pixels for F1550C to account for the larger planetary PSF.

For each cube of case k (Tab. 4), filter λ (Tab. 1) and integration time $t_{\rm int}$ (i.e. 600 s, 1200 s, 1800 s), we measured the photometric uncertainty $(\sigma_F)_{k,\lambda,t_{\rm int}}$ =

$\sqrt{\frac{\sum_{i=1}^{n}(F_i-\bar{F})^2_{k,\lambda,t_{\rm int}}}{n}}$ and signal-to-noise ratio $(\mathrm{SNR})_{k,\lambda,t_{\rm int}} = (\bar{F}/\sigma_F)_{k,\lambda,t_{\rm int}}$ corresponding to each image in the cube. $\bar{F}_{k,\lambda,t_{\rm int}}$ is the mean number of electrons measured over each cube k and i are the images in the cube.

4.3. *About speckles and planetary detection*

To validate a planetary detection it is first necessary to quantify the effect of stellar residuals' noise, and compare it to the planet-to-star contrast of each target, while taking into account the coronagraphic attenuation, which has effect up to an angular distance of about 3″ from the center (see Fig. 5).

To do so we built for each k case a differential coronagraphic image by subtracting the normalized coronagraphic image of the reference star from the normalized coronographic image of the target star. We then measured the standard deviation of the stellar residuals over various annular areas of five pixels width and increasing radius (of one pixel step), all centered on the 4QPM center. For filter F1550C the annular width was set to seven pixels to cover the size of the PSF. We note that, by working on the normalized images (see § 4.1.1) and not on the science images, we quantified only the intensity of the residual speckle noise (i.e. there are no other sources of noise apart from the stellar residual flux due to the offset between star and reference offset, and the telescope jitter). Figure 9 shows the 5 σ stellar residual flux (henceforth labeled as *contrast curves*) for k cases A, B, C, D for each MIRI coronagraphic filter, as a function of the distance from the center of the differential coronagraphic image. Planets lying above a contrast curve are those that can be detected at 5 σ at least. For each case k and filter λ, we measured the signal-to-noise ratio $(\mathrm{SNR}_{\mathcal{S}})_{k,\lambda}$ of the planet-to-star contrast (henceforth referred to as *planetary contrast*) over the speckle residuals' noise $\mathcal{S}$ by dividing the planetary contrast of each planet by the value of the contrast curve at the respective planetary separation. We provide in Appendix A planetary contrast values and in Appendix B contrast curves values for every case k and 4QPM filter.

The intensity of stellar residuals, likewise planetary signal, is proportional to the square root of the integration time, we hence measured the optimized integration time $(t_{\rm max})_{k,\lambda}$ beyond which the planetary signal would not better stand out of speckle residuals noise.
$(t_{\rm max})_{k,\lambda}$ is a function of both filter λ and case k as the stellar residuals' intensity varies for each case k. For the following we focused on speckle residuals of the optimistic case k_A (and therefore we use the notation $t_{\rm max}$ for simplicity). To compute $t_{\rm max}$ we fitted the function $\sqrt{t_{\rm int}}$ to the $(\mathrm{SNR})_{kP,\lambda}$ values, measured for different integration times (see § 4.2) for case k_P and we calculated the time where $(\mathrm{SNR})_{kP,\lambda} = (\mathrm{SNR}_{\mathcal{S}})_{kA,\lambda}$ (Figure 10, left panel). Table 6 reports values of $t_{\rm max}$ with their corresponding signal-to-noise values. Note that we utilized the $(\mathrm{SNR})_{kP,\lambda}$ values of case k_P because this specific case presents no speckle residuals, we could hence extrapolate the pure planetary signal when fitting the function $\sqrt{t_{\rm int}}$. For the same concept it

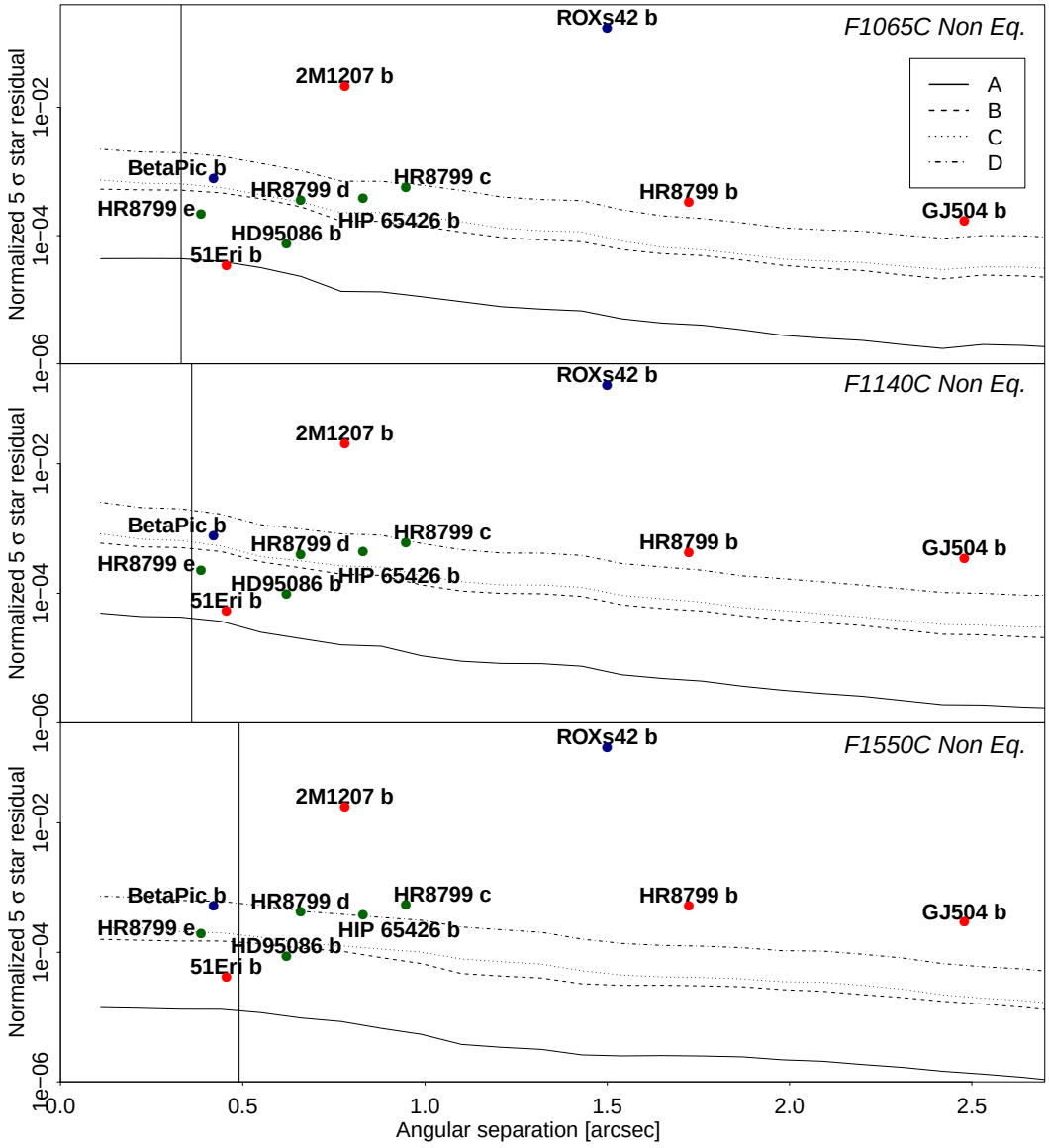

Figure 9. Log-normalized 5 σ contrast curves for the four k cases under study (i.e. A, B, C, D, Tab. 4) and 4QPM filters, as a function of the distance from the coronograph center. The values reported were obtained using differential coronographic images (see § 4.3), they are hence a function of WFE, telescope jitter realizations and stellar offset. No random noise is included. Dots represent the planet-to-star contrast (non-equilibrium case) of each target, attenuated by the coronagraph. The coronagraphic attenuation varies with the distance from the center of the mask, following the coronagraph radial transmission curve (Fig. 5). Colors correspond to the temperature of the target as indicated in the top legend. When a planet is lying above a curve it means that we can detect it at least at 5 σ while, when it is below, the detection is lower than 5 σ. Black vertical lines indicate the IWA value of each filter.

is possible to use the values reported in the table to infer the SNR measured at an integration time different from the one reported, by fitting the same function.

As mentioned above the signal-to-noise ratio is proportional to the square root of the integration time, such as $(\mathrm{SNR})_{kP,\lambda} = \gamma\sqrt{(t_{\max})_{k,\lambda}}$ where γ is a coefficient that depends on the exoplanet analyzed, in term of planetary contrast and angular distance values. Values of $(t_{\max})_{k,\lambda}$ for cases k other than k_A can therefore be deduced from the k_A case using the formula:

$$(t_{\max})_{k,\lambda} = t_{\max}\left(\frac{(\mathrm{SNR_S})_{k,\lambda}}{(\mathrm{SNR_S})_{kA,\lambda}}\right)^2 \quad (1)$$

Using the planetary contrast values (Appendix A) and the contrast curves values (Appendix B), it is hence possible to obtain the $(\mathrm{SNR_S})_{k,\lambda}$ and, consequently, $(t_{\max})_{k,\lambda}$ for each case k. Figure 10, (right panel) shows an example of how the maximal integration times scales as a function of the observational cases k.

Throughout this work we used the telescope background values provided by Glasse et al. (2015), though we tested for a higher background, to leave a margin of error.

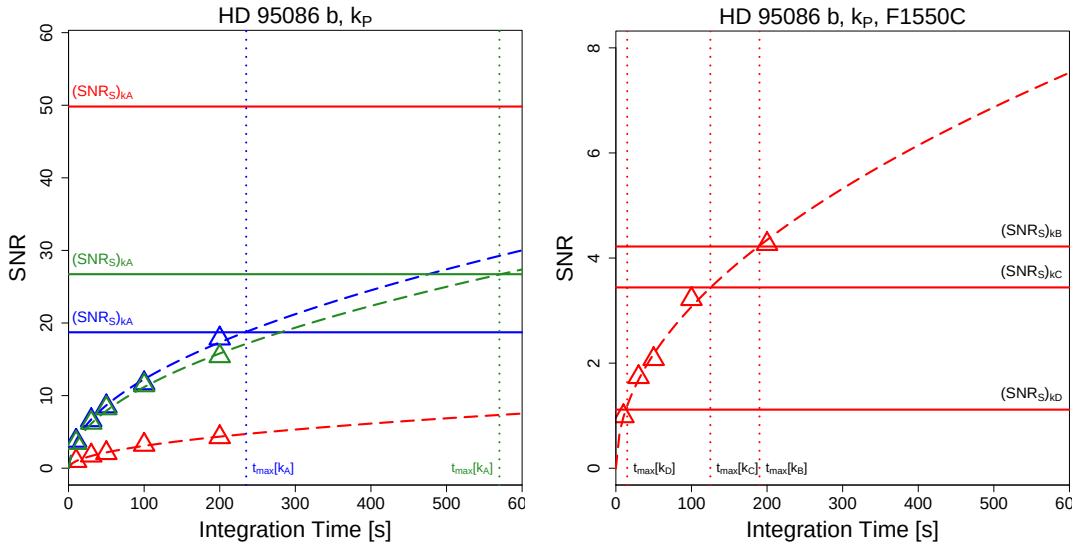

Figure 10. *Left:* SNR_{kP} of HD 95086 b as a function of integration time t_{int}. Colors represent values relative to filter F1065C (*blue*), F1140C (*green*) and F1550C (*red*). Triangles represent the SNR measured in § 4.2 for chemical-equilibrium model, for integration times of t_{int} = 10, 30, 50, 100, 200 s. Dashed lines are the fit to the simulated SNR values ($\sqrt{t_{\mathrm{int}}}$), while solid lines represent the signal-to-noise relative to the speckle intensity of case k_A, $(\mathrm{SNR_S})_{kA}$. The higher the $(\mathrm{SNR_S})_{kA}$, the longer it is possible to integrate and to improve the planetary signal. The integration time $t_{\max}$, defined as the time when SNR_{kP} = $(\mathrm{SNR_S})_{kA}$, is marked by vertical dotted lines and it is reported in Table 6. Note that red$t_{\max}$ = > 7200 s for filter F1550C is outside the plot. *Right:* Same as the left panel, but only for filter F1550C. Here solid lines represent the signal-to-noise relative to the speckle intensity of case k_B: $(\mathrm{SNR_S})_{kB}$, k_C: $(\mathrm{SNR_S})_{kC}$, and k_D: $(\mathrm{SNR_S})_{kD}$. Note how $t_{\max}$ scales, depending on the observational case ($(\mathrm{SNR_S})_{kA}$ does not appear due to a different y-axis scale, which was employed for clarity reasons).

We simulated the case k_P of HIP 65426 b (i.e. faintest coronagraphic target star) for filter F1550C (i.e. with highest background among the 4QPM filters) non-equilibrium chemistry, increasing background values by Glasse et al. (2015) of 50%. We found that $t_{\rm max} > 7200$ s also for the increased background case. More specifically: at $t_{\rm int}$ = 1200 s we measured a $\rm SNR_{+50\%} = 10$ (previously SNR = 13), and at $t_{\rm int}$ = 2400 s we measured a $\rm SNR_{+50\%} = 15$ (previously SNR = 18.)

5. DISCUSSION

We note that in our analysis no advanced post-processing techniques (e.g. PCA, Choquet et al. 2016) have been applied: results are obtained by directly using the science image obtained after the subtraction of the reference image from the target image and by knowing the exact position of the planet on the image. The use of the currently known modern post-processing techniques will improve the planetary SNR for cases k_B, k_C and k_D reaching up to the k_A level, where optimal stellar subtraction is achieved (even though there are both jitter effects and some residual stellar photon noise, because such noise is different for target star and reference). As an example of the improvement we can have with modern post-processing techniques we refer to the work by Soummer et al. (2014) which presents a comparison between the contrast achieved with a classical reference subtraction and with the small-grid dither technique. At 1″ and F1140C, while the classical subtraction yields a 5 σ contrast of the order of $\sim 10^{-3.4}$ (i.e. in between our 5 σ k_C and k_D cases), the 9-point dithers (dither step = 10 mas) returns a 5 σ contrast of $\sim 10^{-5.6}$, meaning an improvement factor of ≈ 150. We note that the value of the 9-point dither contrast is smaller than the one achieved in our k_A case. Though, in their simulations the telescope jitter, which is the limiting contrast factor in our case k_A, was not taken into account. We can thus conclude that case k_A provides a good limit of what can be achieved with small-grid dither technique, meaning, for instance, that our k_D contrast could be improved at levels very close to the k_A one.

We remind the reader that k_P is not realistic as it does not include the telescope jitter noise.

5.1. *Planets' detectability*

As explained in § 4.3 a planetary detection is feasible when the planetary contrast, attenuated by the coronagraph, is larger than the speckle contrast; this dimension, called $(\rm SNR_S)_{k,\lambda}$, has been quantified for each planet with respect to all the cases k of speckles' residuals and filters λ (Fig. 9), and needs to be larger than 5 to assure a planetary detection. Table 6 reports the values of $(\rm SNR_S)_{kA}$ for all the planets observed in coronagraphic mode. We remind the reader that contrast curves have been estimated by computing the standard deviation of the speckle residuals over various annular areas around the 4QPM center (see § 4.3). While some sources appear easily detectable due to their intrinsic luminosity (e.g. 2M1207 b, ROXs42

Table 6. Measured integration time $t_{\max}$ beyond which planetary signal would not better stand out of case k_A speckle noise. $t_{\max}$ value corresponds to the integration time when the signal-to-noise of case k_P (i.e. where Poisson noise and background are the only sources of noise: no jitter and no offset between target star and reference are included) is equal to the signal-to-noise of the planetary contrast versus the speckle residuals of case k_A, hence when $\mathrm{SNR}_{kP} = (\mathrm{SNR}_{\mathcal{S}})_{kA}$. The equilibrium and non equilibrium cases are represented by the "eq" and "neq" strings, respectively.

Planet		F1065C		F1140C		F1550C	
		$(\mathrm{SNR}_{\mathcal{S}})_{kA}$	$t_{\max}$[s]	$(\mathrm{SNR}_{\mathcal{S}})_{kA}$	$t_{\max}$ [s]	$(\mathrm{SNR}_{\mathcal{S}})_{kA}$	$t_{\max}$[s]
β Pictoris b	eq	98	15	102	20	198	700
	neq	95	15	102	20	198	680
51 Eri b	eq	2	25	7	40	15	1020
	neq	4	25	8	40	16	995
GJ 504 b	eq	152	4180	570	> 7200	227	> 7200
	neq	447	5185	749	> 7200	245	> 7200
HD 95086 b	eq	19	235	27	570	26	> 7200
	neq	14	210	22	565	22	> 7200
2M1207 b	eq	625	> 7200	528	> 7200	144	> 7200
	neq	542	> 7200	430	> 7200	123	> 7200
ROXs42 b	eq	820	> 7200	663	> 7200	196	> 7200
	neq	820	> 7200	684	> 7200	196	> 7200
HIP 65426 b	eq	162	> 7200	147	> 7200	34	> 7200
	neq	129	> 7200	124	> 7200	30	> 7200
HR 8799 b	eq	771	>7200	682	> 7200	296	> 7200
	neq	402	6120	442	> 7200	203	> 7200
HR 8799 c	eq	293	950	289	1995	206	> 7200
	neq	235	855	245	1805	192	> 7200
HR 8799 d	eq	99	1070	124	2110	101	> 7200
	neq	78	1000	100	1815	92	> 7200
HR 8799 e	eq	31	990	33	1150	–	–
	neq	27	950	29	1095	–	–

NOTE—For those cases where $t_{\max} > 7200$ s, we report the SNR measured at exactly 7200 s.

b), for others the prospect of a detection strongly varies with the case k in which the telescope is observing.

51 Eri b, HD 95086 b and HR 8799 e have relatively small $(\mathrm{SNR}_{\mathcal{S}})_{kA}$ and their detection is more difficult, even with the coronagraph.

We note that the parameter that plays a major effect in a coronagraphic observation is the offset between the target star and the reference. Hence, for sources with low SNR_S, specific coronagraphic target acquisition and operations, such as the small grid dither concept, in conjunction with sophisticated image analysis algorithms for optimizing the PSF subtraction (e.g. LOCI: Lafrenière et al. 2007; KLIP: Soummer et al. 2012), are necessary (Soummer et al. 2014; Lajoie et al. 2016, and references therein).

In our analysis 51 Eri b cannot be detected at 5 σ in filter F1065C in the optimistic case observation (k_A) because it is buried in the speckle residuals. Note that beside detectability issues, it is possible that the planet is moving towards the star (De Rosa et al. 2015), meaning that there is the possibility that it will not be observable by MIRI coronagraph in 2020, after JWST launch, being within the IWA.

The planet HD 95086 b is detectable at 5 σ only in case k_A for all filters (both chemical states).

The planet β Pictoris b can be detected at 5 σ in filter F1065C in all cases but case k_D. We note that a 5 σ detection is possible at F1550C for cases k_A, k_B, k_C despite the planet being inside λ/D ($(SNR_S)_{kA} = 198$, Fig. 9, Tab. 6). This means that it is possible to push MIRI observations also for those planets with angular distance smaller than the IWA (here $0.42''$ compared to $\lambda/D = 0.49''$). By design, the 4QPM does not provide an abrupt cut at the IWA level, but instead a smooth transition which may allow the detection of planets within the IWA. However, the planet image is significantly non-linearly affected by the coronagraphic mask and so such a detection inside the IWA cannot be made in practice at any separations. This remains to be quantified yet as it is out of scope of this manuscript.

Concerning the HR 8799 system the only planet detectable in any condition is HR 8799 b. HR 8799 c detection in k_D is borderline for F1065C and F1140C both equilibrium and non-equilibrium cases. HR 8799 d can be detected at 5 σ for all the cases but case k_D in filters F1065C and F1140C (equilibrium case). For the non-equilibrium case the detection is difficult also in F1065C, k_C. In F1550C, case k_D, the detection is borderline for both chemical states. HR 8799 e is only visible in filters F1065C and F1140C, case k_A. With only a classical reference subtraction technique the planet is not directly detectable in filter F1550C as the IWA is too large and also because, at this wavelength, its PSF is highly contaminated/covered by the larger PSFs of the other planets.

GJ 504 b is always detectable at 5 σ apart from k_D, F1065C equilibrium case.

For the HIP 65426 b simulation we used the Exo-REM model at $T_P = 1300$ K which is the minimal T_P estimated by Chauvin et al. 2017, meaning that we measure the inferior limit of $(SNR_S)_{kA}$ and that larger signal-to-noise could be achieved if the planet is warmer than 1300 K ($(SNR_S)_{kA} = 34$ for F1550C and integration time $t_{\rm int}$ = 7200 s for the equilibrium case). A 5 σ planetary detection is not possible only for

case k_D in filters F1065C and F1140C (both equilibrium and non-equilibrium cases). For F1550C the detection becomes challenging also for k_D, both chemical states.

We note that these simulations were performed with a specific angular position (i.e., 45°), in order to maximize the planetary flux. The results are the outcome of a optical path with specific parameters (such as the amplitude of the telescope defocus, the stellar pupil shift, the pupil rotation, etc., see Tab. 5) which can vary when the telescope will be in orbit.

5.2. *NH_3 in an exoplanetary atmosphere.*

The ammonia absorption band (centered at $\lambda = 10.65$ μm) is visible in the synthetic spectra of planets whose temperature is $T_P \lesssim 1200$ K and it can be a useful index of both planetary temperature and atmospheric chemical equilibrium state. While for the temperature index the general rule is that the cooler the planet, the stronger the NH_3 band, for the chemical equilibrium index it is important to distinguish two regimes: one with temperature $T_P < 1000$ K and one with 1000 K $< T_P \lesssim 1200$ K. This difference is due to the vertical profile of NH_3 at thermochemical equilibrium, which increases with height in the lower atmosphere, reaches a minimum, and then increases with height at higher levels. This behavior results from a competition between decreasing temperature (that favors NH_3) and decreasing pressure (that favors N_2) with height. For objects with relatively low T_P (GJ 504 b and 51 Eri b), the NH_3 equilibrium abundance at the quench level is smaller than that in the emitting region (aka. photosphere), leading to a stronger absorption feature in the equilibrium case. The situation is opposite in the second regime (e.g. HR 8799 b), as the NH_3 abundance profile at equilibrium decreases between the quench level and the emitting region. Figure 11 shows an example for the case of GJ 504 b, whose temperature put the planet in the first regime ($T_P = 544$ K).

In our coronagraphic target list 2M1207 b, 51 Eri b, GJ 504 b, HD 95086 b, HR 8799 b, c, d, e have such temperatures to potentially host ammonia in their atmosphere. In the event that this molecule is present and abundant in the atmosphere, we would observe an increase of flux from filter F1065C to filter F1140C. On the other hand, for a relatively low abundance of NH_3, it was thought to use the combination of F1550C and F1140C observations, to retrieve the ammonia line and its abundance, by fitting to the observations a black body curve.

We applied this method in our analysis in order to validate a possible MIRI/4QPM detection of NH_3 in the atmosphere of the above mentioned exoplanets. We produced a black body (BB) curve at the planetary temperature T_P of reference (Tab. 2), we then integrated this BB curve on the 4QPM coronagraphic filters, obtaining three BB data points centered on the 4QPM filters' central wavelengths λ_C. We then corrected each of these three BB data points for the respective coronagraphic attenuation and filter transmission values (these corrections are necessary because they are wavelength dependent). Therefore we minimized the flux offset between the two BB points at λ_2

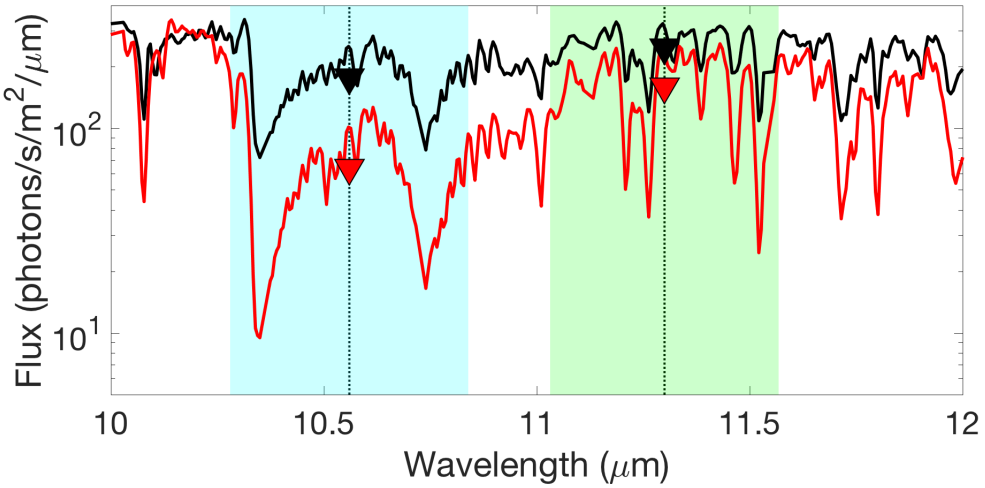

Figure 11. Exo-REM models for GJ 504 b equilibrium case (*red*) and non-equilibrium case (*black*). Note that, given the temperature of T_P = 554 K , the equilibrium model has a deeper NH_3 feature than the non-equilibrium model. Black and red triangles mark the integrated flux in each filter. Shaded areas mark the F1065C (*light blue*) and F1140C (*green*) filters' range, while dashed vertical lines mark the filters' central wavelength.

Planet	eq	neq
2M1207 b	3 σ	4 σ
GJ 504 b	98 σ	66 σ
HR 8799 b	16 σ	30 σ
HR 8799 d	–	3 σ

Table 7. Significance of ammonia detection for case k_A when the planet has $SNR_S > 5$ in all 4QPM filters at t_{int} = 1800 s for both chemical state of equilibrium ("eq") and non-equilibrium ("neq") obtained using a black-body approximation

= 11.40 μm and λ_3 = 15.50 μm and their respective simulated ones. The uncertainty on this minimization is given by $\sigma_M = \sqrt{\sigma^2_{\lambda_2} + \sigma^2_{\lambda_3}}$ where $\sigma^2_{\lambda_2}$ and $\sigma^2_{\lambda_3}$ are the observed variance at λ_2 and λ_3, respectively.

We then compared the simulated data point with the black body point at λ_1: in the case where the simulated flux is dimmer and not consistent with the equivalent BB one, it means that we are detecting an absorption in the planetary spectra, in this specific case the NH_3 one. The significance σ_{NH3} of this detection has been measured as:

$$\sigma_{NH3} = \frac{(F_{BB})_{\lambda_1} - (F_{obs})_{\lambda_1}}{\sigma_{tot}} \tag{2}$$

where $(F_{BB})_{\lambda_1}$ is the BB point calculated at λ_1, $\sigma_{tot} = \sqrt{\sigma^2_M + \sigma^2_{\lambda_1}}$, and where $(F_{obs})_{\lambda_1}$ and $\sigma^2_{\lambda_1}$ are the observed flux and variance at λ_1, respectively.

We note that we are assuming no error on the black body curve, though this error will have to be accounted for when performing the same analysis on real data.

For an integration time of t_{int} = 1800 s, our analysis shows a clear detection (i.e. $\sigma_{NH3} > 5$) of ammonia in the atmosphere of HR 8799 b and GJ 504 b in both chemical

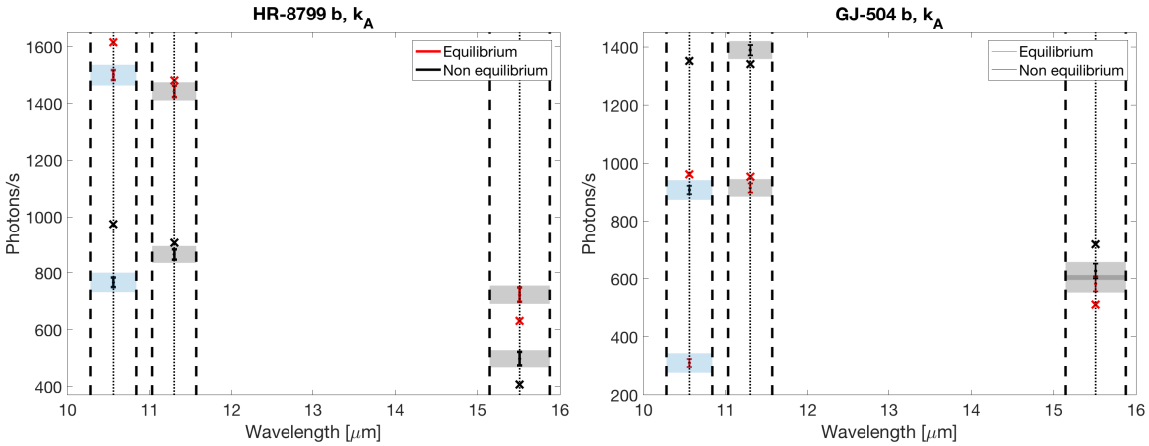

Figure 12. Case k_A simulated flux (*errorbars*) vs blackbody flux (*crosses*) of HR 8799 b (*left*) and GJ 504 b (*right*). The 5 σ errorbars are plotted for both equilibrium (*red*) and non equilibrium (*black*) cases. Shaded areas correspond to 5 σ_M (*grey*) and 5 $\sigma_{\rm tot}$ (*blue*). Dashed vertical lines mark the filters wavelength range, while dotted vertical lines mark filters' central wavelength.

states. For 2M1207 b (both chemical states) and HR 8799 d (only non-equilibrium) the significance is $3 \leq \sigma_{\rm NH3} < 5$. Table 7 reports the significance of the ammonia detection for those planets whose $({\rm SNR_S})_{k_A} > 5$ in all the three coronagraphic filters.

Figure 12 shows our results for HR 8799 b and GJ 504 b, k_A. We observe that for the HR 8799 b case the black body point and the observed point at F1550C (both chemical states) are not consistent with each other. The reason for this lies in the fact that the Exo-REM model and the BB curve at temperature T_P differ. It therefore follows that it not always possible to approximate (to the first-order) a planetary spectrum to a black body curve. This approach risks to give imprecise results such as under/over-estimation of both ammonia detection significance and its absolute abundance. For this reason we strongly suggest the use of radiative transfer models possibly coupled with *inverse retrievals* techniques (e.g. Irwin et al. 2008; Line et al. 2013; Waldmann et al. 2015; Rocchetto et al. 2016) to objectively determine the absolute gas abundances .

A specific study presenting the use of retrievals methods on MIRI data will be presented in a forthcoming paper.

5.3. *Other molecules*

Several molecules other than NH_3 have features in the MIRI wavelength range (i.e. CH_4, PH_3, CO_2, H_2O; e.g. Fig. 18 by Baudino et al. 2017 concerning the spectrum of VHS 1256-1257 b). MIRI spectroscopic observations, when possible, can give access to those lines. A high signal-to-noise ratio close or higher than 100 can be achieved in one hour (see Tab. 8). We show in Fig. 13 the extracted LRS spectrum of 2M2236+4751 b for one hour integration. Such observations will allow us to distinguish between equilibrium or non-equilibrium chemistry in the atmosphere of an exoplanet.

Table 8. Signal over noise ratio for various sources observed with the Low Resolution Spectroscopic mode of MIRI as calculated with the JWST exposure time calculator (ETC)[a]. Effects not taken into account, such as on how well the star signal at the position of the planet can be removed (especially for 2M1207 b and GJ 504 b) or calibration precision, will limit the SNR achievable to a value lower than that quoted here.

Sources	SNR at 5 μm	SNR at 8 μm	SNR at 11 μm
2M1207 b	292	130	45
2M2236+4751 b	230	58	25
GJ 504 b	290	42	29
HD 106906 b	323	134	35
ROXs42B b	417	198	55
VHS 1256-1257 b	880	351	266

NOTE— (a) https://jwst.etc.stsci.edu/

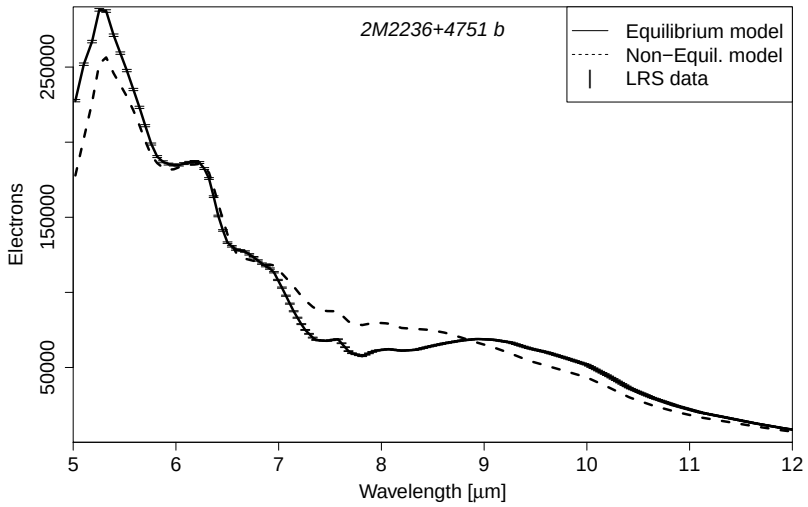

Figure 13. Extracted spectrum of 2M2236+4751 b (equilibrium case) after one hour of simulated observation with the MIRI Low Resolution Spectroscopic mode (using the JWST ETC); overplotted the 3 σ noise. The ETC sources of noise are: photon noise (source + background), detector noise, dark current noise and flat field errors; detector drifts effect are not taken into account. Synthetic models (see legend) have been plotted for comparison.

5.4. *Synergies between MIRI and NIR instruments*

As previously mentioned one of the known problems of planetary atmospheric characterization is the limited wavelength coverage in which current instruments work. Measurements limited to a narrow spectral range yield significant uncertainties which do not allow to break degeneracy between planetary parameters.

This is where MIRI, conjointly with NIRCam[5], plays a key role: by extending planetary observations to the mid-infrared it will be possible to constrain the atmospheric properties with higher precision.

We report here HR 8799 b as a test case to show the performances of MIRI/4QPM in term of accurate modeling of the exoplanetary atmosphere features.
We generated a family of Exo-REM models ($\Delta\lambda$ = 0 - 28 μm) fitting the planetary photometric observations reported in Bonnefoy et al. (2016) to have a group of models reproducing the observations at 1σ (Fig. 14, top panel). We only selected photomet-

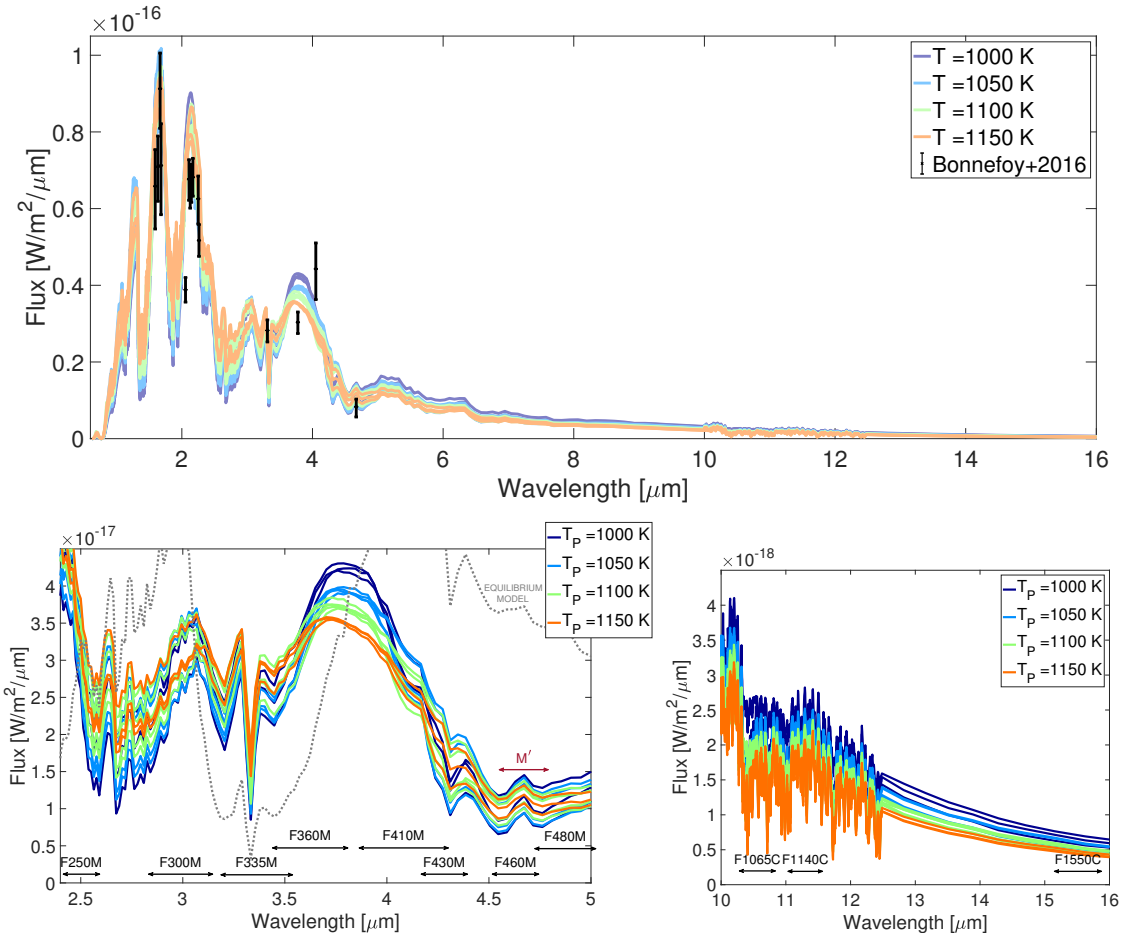

Figure 14. HR 8799 b non-equilibrium synthetic models (measured at Earth) fitting the available photometric NIR observations by Bonnefoy et al. (2016)(*top*) as seen in the NIRCam long wavelength channel (*bottom left*) and MIRI coronagraphic filters (*bottom right*). In the bottom left plot we show the available medium NIRCam filters allowed for coronagraphic imaging (*black*) and Keck/NIRC2 M′ filter (*red*). Dotted line shows the equilibrium model (T_P = 1200 K, log(g) = 5.2) used in the simulations. In the bottom right plot we mark the 4QPM filters spectral range. We note that in the F1065C and F1140C wavelength range all models are at high resolution to prevent the under-sampling of the ammonia feature in the observations simulation.

[5] https://jwst-docs.stsci.edu/display/JTI/NIRCam+Overview, the JWST near-IR camera with coronagraphic capabilities

ric data in order to analyze a representative case.

The fitting models resulted to be only non-equilibrium chemistry ones spanning temperatures from 1000 to 1150 K, surface gravity values $\log(g)$ = 4.4 - 4.8 and metallicity values z = 0 and +0.5 dex. Note that both HR 8799 b equilibrium and non-equilibrium models, previously used in the science image simulations, are not part of this family of models because of different sets of data used for the minimization process (see § 3).

On a general level, by using the JWST/NIRCam F460M or/and F480M filters, and/or the M′-band filter in the Adaptive Optic Keck/NIRC2 near-infrared narrow-field camera (McLean and Sprayberry 2003), it will be possible to distinguish between chemical equilibrium and non-equilibrium state of the atmosphere of a directly imaged exoplanet. In this spectral range (4-5 μm) there are overlapping features of at least three molecules, PH_3, CO and CO_2, whose abundances are impacted by non-equilibrium chemistry (Baudino et al. 2017, Sec. 6.4). Figure 14 bottom left panel shows the different emission spectra in this particular wavelength range, in the cases whether the atmosphere is in chemical equilibrium or not.

When knowing the chemical state we can move to the mid-infrared, in the MIRI bands, to retrieve the effective temperature of the planet. To test the precision achievable on this parameter with MIRI we integrated each synthetic model over the 4QPM filters and we added the corresponding uncertainties on the flux measured in § 4.2 at $t_{\max}$ = 4000 s for the photon noise case k_P. Figure 15 shows the 5 σ resulting measurements for each filter, with the corresponding temperature, surface gravity and metallicity. We find that, using filter F1140C, it is possible to disentangle models at better than ΔT = 100 K apart from each other. Though, by combining the data-points at F1140C and F1550C it will be possible to better constrain the temperature and the bolometric luminosity of the planet due to the high SNR in these filters (Tab. 6, Fig. 14 bottom right). This said we notice that various degeneracies between temperature, surface gravity and metallicity persist. A clear example can be found in Fig. 15 around $F_{\rm obs} = 1.9 \cdot 10^{-18}$ W m^{-2} at F1065C or between $F_{\rm obs} = 5 \cdot 10^{-19}$ W m^{-2} and $F_{\rm obs} = 6 \cdot 10^{-19}$ W m^{-2} at F1550C, where various temperature, surface gravity and metallicity values are consistent with one another at the 5 σ level.
One way to start breaking these degeneracies is to get spectroscopic observations in the 3.4 - 4.1 μm wavelength range (i.e. the L′ band) to determine the planetary temperature. Even though this will not be sufficient for breaking all the degeneracies, it will allow us to discern more data-points in the mid-infrared. Having various observations that homogeneously cover a wide spectral range is key for mapping the planetary spectrum. Furthermore, given the increased complexity in the interpretation of the spectrum due to high accuracy data, it is necessary to maximize the objectivity of the analysis from the start by not assuming anything about the atmospheres composition

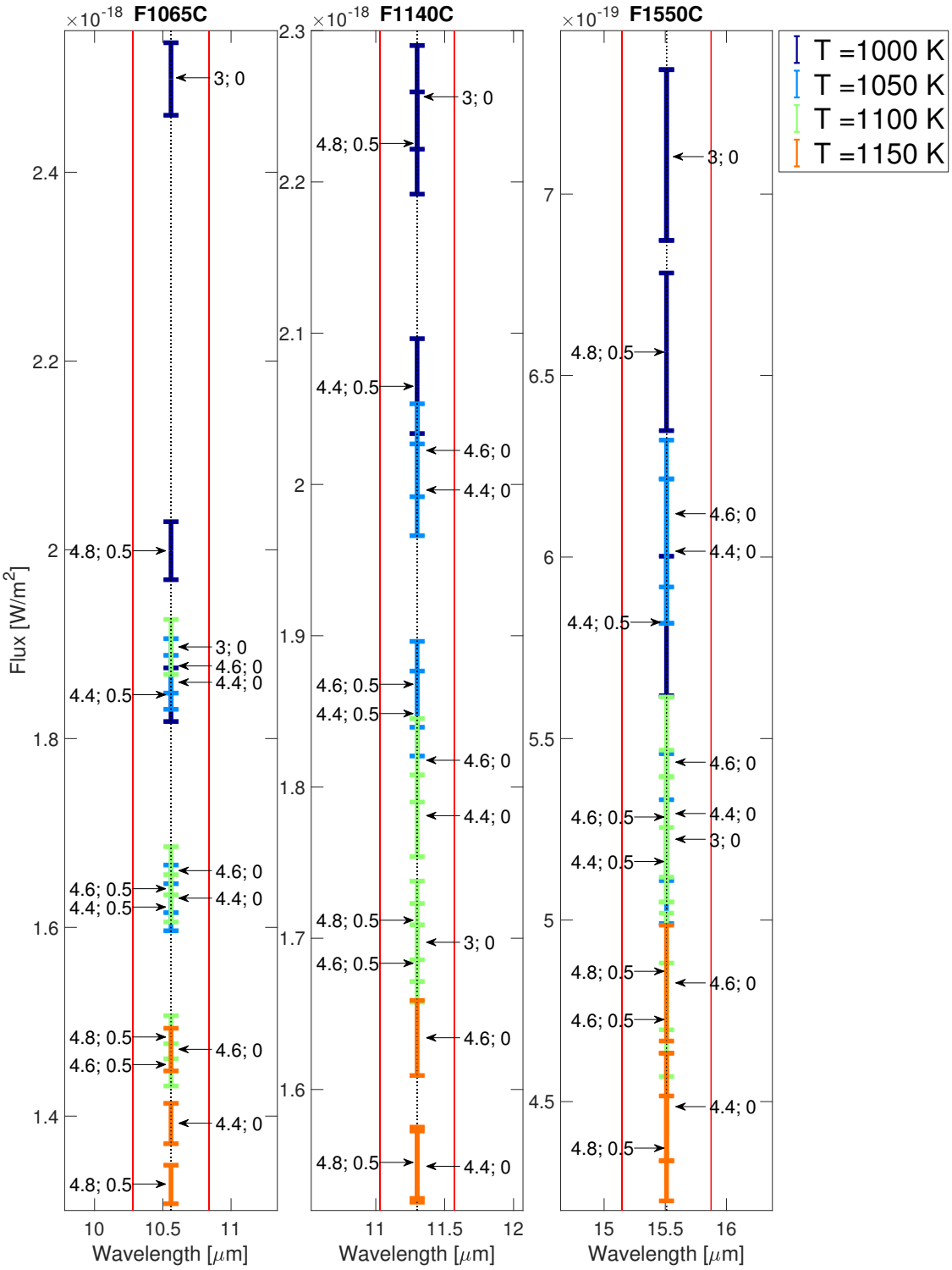

Figure 15. HR 8799 b synthetic models integrated over the 4QPM filters with 5 σ error. Uncertainties are the ones calculated for case k_P at $t_{\max} = 4000$ s. Colors mark the effective temperature of the models, while arrows correspond to the equivalent surface gravity [cgs] followed by the metallicity information.

and structure. For this reason we recommend again the use of inverse atmospheric retrieval modeling for objectively interpreting the data.

6. CONCLUSIONS

We discussed here the simulated Mid-Infrared instrument (MIRI) coronagraphic observations for a set of known directly imaged exoplanets, whose emission spectrum has been calculated using the Exoplanet Radiative-convective Equilibrium Model. The sample of analyzed objects presented effective temperatures ranging from 544 K to 1975 K, planet-to-star contrasts from 3.88 mag to 10.07 (measured at 15.50 μm), and angular separations from 0.42″ to 8.06″. We provide planetary contrasts for each target and MIRI coronagraphic filter.

(1) We studied the effect of the coronagraphic transmission as a function of the MIRI angular position (PA) of the planet, providing a coronagraphic transmission map over an area of 8″ x 8″ centered on the coronagraphic mask. When planning MIRI observations, if the observational window allows it, we suggest to set the planet at either one of the the MIRI PA = 45°, 135°, 225°, 315°.

(2) We examined the detectability of each target as a function of the four-quadrant phase mask (4QPM) filters and various observing telescope conditions i.e. by taking into consideration variations of:

(i) offsets between the target star and the reference star: either 0 mas, 3 mas or 14 mas.
(ii) wave-front-error (WFE): either 130 nm rms or 204 nm rms.
(iii) jitter amplitude: either 1.6 mas or 7 mas.

More specifically we analyzed four combinations of these parameters, resulting in one optimistic observation, a pessimistic one and two intermediate observations. For each combination and each 4QPM filter we provided the corresponding contrast curves.

(3) We analyzed a fifth observational case whose only source of noise is Poisson noise. For this specific case we measured the signal-to-noise (SNR) and integration times for each coronagraphic target. For an integration time $t_{\rm int}$ = 35 s the SNR spans values from 3 to 37 depending on the planetary contrast level (the highest or lowest in our target list, respectively).
We tested for the effect of a 50% higher background, at 15.50 μm, by studying the case of HIP 65426 b, whose star is the faintest among our targets. We found small differences: The $\rm SNR_{50\%}$ measured $\rm SNR_{50\%}$ = 15 at $\rm t_{int}$ = 2400 s, compared to a SNR = 18, for the same integration time.

(4) We showed that planetary detection strongly depends on the JWST in-flight performances and that a perfect stellar removal is highly necessary to obtain the best science results. For this reason we overall recommend the use of small grid dither

concept while observing a target, in conjunction with sophisticated image-analysis algorithms for optimizing the PSF subtraction.

(5) We note that ammonia is a useful indicator of both planetary effective temperature and atmospheric chemical equilibrium state. We tested for the detectability of this molecule in the atmosphere of the coolest planets of our target list, predicting a possible NH_3 detection in HR 8799 b, d, GJ 504 b and 2M1207 b. The significance of this detection ranges from 3 σ to 98 σ, depending on the planetary contrast and effective temperature.

(6) We have shown that several exoplanets detected by direct imaging can be observed using MIRI spectroscopy mode. Such observations will bring information not only on NH_3 but also on CH_4, H_2O, CO_2, PH_3 where very high SNR (» 100) can be obtained.

(7) MIRI, together with NIRCam, will provide strong constraints on the spectral characterization of young giant planets in wide orbits, pinning down the effective temperature and bolometric luminosity to an unprecedented accuracy.
The use of retrieval modeling techniques is advisable to maximize the objectivity of the analysis to infer the properties of exoplanetary atmospheres, including molecular abundances and temperature profiles. A specific study presenting the use of retrievals methods on MIRI data will be presented in a forthcoming paper.

C.D. acknowledges support from the LabEx P2IO, the French ANR contract 05-BLAN-NT09-573739, the Centre National d'etudes Spatiales (CNES) post-doctoral funding project and the P2IO LabEx (ANR-10-LABX-0038) in the framework ≪Investissements d'Avenir≫(ANR-11-IDEX-0003-01). J. L. B. acknowledges the support of the UK Science and Technology Facilities Council. All simulations presented in this work were performed in GDL (https://github.com/gnudatalanguage/gdl/). The authors would like to thank the anonymous referee whose comments and suggestions helped to improve and clarify this paper.

REFERENCES

V. Bailey, T. Meshkat, M. Reiter, K. Morzinski, J. Males, K. Y. L. Su, P. M. Hinz, M. Kenworthy, D. Stark, E. Mamajek, R. Briguglio, L. M. Close, K. B. Follette, A. Puglisi, T. Rodigas, A. J. Weinberger, and M. Xompero. HD 106906 b: A Planetary-mass Companion Outside a Massive Debris Disk. *ApJL*, 780:L4, January 2014. doi:10.1088/2041-8205/780/1/L4.

I. Baraffe, D. Homeier, F. Allard, and G. Chabrier. New evolutionary models for pre-main sequence and main sequence low-mass stars down to the hydrogen-burning limit. *A&A*, 577: A42, May 2015. doi:10.1051/0004-6361/201425481.

J.-L. Baudino, B. Bézard, A. Boccaletti, M. Bonnefoy, A.-M. Lagrange, and R. Galicher. Interpreting the photometry and spectroscopy of directly imaged planets: a new atmospheric model applied to β Pictoris b and SPHERE observations. *A&A*, 582:A83, October 2015. doi:10.1051/0004-6361/201526332.

J.-L. Baudino, P. Mollière, O. Venot, P. Tremblin, B. Bézard, and P.-O. Lagage. Toward the Analysis of JWST Exoplanet Spectra: Identifying Troublesome Model Parameters. *ApJ*, 850:150, December 2017. doi:10.3847/1538-4357/aa95be.

J.-L. Beuzit, M. Feldt, K. Dohlen, D. Mouillet, P. Puget, F. Wildi, L. Abe, J. Antichi, A. Baruffolo, P. Baudoz, A. Boccaletti, M. Carbillet, J. Charton, R. Claudi, M. Downing, C. Fabron, P. Feautrier, E. Fedrigo, T. Fusco, J.-L. Gach, R. Gratton, T. Henning, N. Hubin, F. Joos, M. Kasper, M. Langlois, R. Lenzen, C. Moutou, A. Pavlov, C. Petit, J. Pragt, P. Rabou, F. Rigal, R. Roelfsema, G. Rousset, M. Saisse, H.-M. Schmid, E. Stadler, C. Thalmann, M. Turatto, S. Udry, F. Vakili, and R. Waters. SPHERE: a 'Planet Finder' instrument for the VLT. In *Ground-based and Airborne Instrumentation for Astronomy II*, volume 7014 of *Proc. SPIE*, page 701418, July 2008. doi:10.1117/12.790120.

A. Boccaletti, P.-O. Lagage, P. Baudoz, C. Beichman, P. Bouchet, C. Cavarroc, D. Dubreuil, A. Glasse, A. M. Glauser, D. C. Hines, C.-P. Lajoie, J. Lebreton, M. D. Perrin, L. Pueyo, J. M. Reess, G. H. Rieke, S. Ronayette, D. Rouan, R. Soummer, and G. S. Wright. The Mid-Infrared Instrument for the James Webb Space Telescope, V: Predicted Performance of the MIRI Coronagraphs. *PASP*, 127:633, July 2015. doi:10.1086/682256.

M. Bonnefoy, et al., and . .

M. Bonnefoy, A. Boccaletti, A.-M. Lagrange, F. Allard, C. Mordasini, H. Beust, G. Chauvin, J. H. V. Girard, D. Homeier, D. Apai, S. Lacour, and D. Rouan. The near-infrared spectral energy distribution of β Pictoris b. *A&A*, 555:A107, July 2013. doi:10.1051/0004-6361/201220838.

M. Bonnefoy, A. Zurlo, J. L. Baudino, P. Lucas, D. Mesa, A.-L. Maire, A. Vigan, R. Galicher, D. Homeier, F. Marocco, R. Gratton, G. Chauvin, F. Allard, S. Desidera, M. Kasper, C. Moutou, A.-M. Lagrange, J. Antichi, A. Baruffolo, J. Baudrand, J.-L. Beuzit, A. Boccaletti, F. Cantalloube, M. Carbillet, J. Charton, R. U. Claudi, A. Costille, K. Dohlen, C. Dominik, D. Fantinel, P. Feautrier, M. Feldt, T. Fusco, P. Gigan, J. H. Girard, L. Gluck, C. Gry, T. Henning, M. Janson, M. Langlois, F. Madec, Y. Magnard, D. Maurel, D. Mawet, M. R. Meyer, J. Milli, O. Moeller-Nilsson, D. Mouillet, A. Pavlov, D. Perret, P. Pujet, S. P. Quanz, S. Rochat, G. Rousset, A. Roux, B. Salasnich, G. Salter, J.-F. Sauvage, H. M. Schmid, A. Sevin, C. Soenke, E. Stadler, M. Turatto, S. Udry, F. Vakili, Z. Wahhaj, and F. Wildi. First light of the VLT planet finder SPHERE. IV. Physical and chemical properties of the planets around HR8799. *A&A*, 587:A58, March 2016. doi:10.1051/0004-6361/201526906.

Mickael Bonnefoy, A Zurlo, JL Baudino, P Lucas, D Mesa, A-L Maire, A Vigan, R Galicher, D Homeier, F Marocco, et al. First light of the vlt planet finder sphere-iv. physical and chemical properties of the planets around hr8799. *Astronomy & Astrophysics*, 587:A58, 2016.

P. Bouchet, M. García-Marín, P.-O. Lagage, J. Amiaux, J.-L. Auguéres, E. Bauwens, J. A. D. L. Blommaert, C. H. Chen, Ö. H. Detre, D. Dicken, D. Dubreuil, P. Galdemard, R. Gastaud, A. Glasse, K. D. Gordon, F. Gougnaud, P. Guillard, K. Justtanont, O. Krause, D. Leboeuf, Y. Longval, L. Martin, E. Mazy, V. Moreau, G. Olofsson, T. P. Ray, J.-M. Rees, E. Renotte, M. E. Ressler, S. Ronayette, S. Salasca, S. Scheithauer, J. Sykes, M. P. Thelen, M. Wells, D. Wright, and G. S. Wright. The Mid-Infrared Instrument for the James Webb Space Telescope, III: MIRIM, The MIRI Imager. *PASP*, 127: 612, July 2015. doi:10.1086/682254.

B. P. Bowler, M. C. Liu, D. Mawet, H. Ngo, L. Malo, G. N. Mace, J. N. McLane, J. R. Lu, I. I. Tristan, S. Hinkley, L. A. Hillenbrand, E. L. Shkolnik, B. Benneke, and W. M. J. Best. Planets around Low-mass Stars (PALMS). VI. Discovery of a Remarkably Red Planetary-mass Companion to the AB Dor Moving Group Candidate 2MASS J22362452+4751425*. *AJ*, 153:18, January 2017. doi:10.3847/1538-3881/153/1/18.

G. Chauvin, A.-M. Lagrange, C. Dumas, B. Zuckerman, D. Mouillet, I. Song, J.-L. Beuzit, and P. Lowrance. A giant planet candidate near a young brown dwarf. Direct VLT/NACO observations using IR wavefront sensing. *A&A*, 425: L29–L32, October 2004. doi:10.1051/0004-6361:200400056.

G. Chauvin, S. Desidera, A.-M. Lagrange, A. Vigan, R. Gratton, M. Langlois, M. Bonnefoy, J.-L. Beuzit, M. Feldt, D. Mouillet, M. Meyer, A. Cheetham, B. Biller, A. Boccaletti, V. D'Orazi, R. Galicher, J. Hagelberg, A.-L. Maire, D. Mesa, J. Olofsson, M. Samland, T. O. B. Schmidt, E. Sissa, M. Bonavita, B. Charnay, M. Cudel, S. Daemgen, P. Delorme, P. Janin-Potiron, M. Janson, M. Keppler, H. Le Coroller, R. Ligi, G. D. Marleau, S. Messina, P. Mollière, C. Mordasini, A. Müller, S. Peretti, C. Perrot, L. Rodet, D. Rouan, A. Zurlo, C. Dominik, T. Henning, F. Menard, H.-M. Schmid, M. Turatto, S. Udry, F. Vakili, L. Abe, J. Antichi, A. Baruffolo, P. Baudoz, J. Baudrand, P. Blanchard, A. Bazzon, T. Buey, M. Carbillet, M. Carle, J. Charton, E. Cascone, R. Claudi, A. Costille, A. Deboulbe, V. De Caprio, K. Dohlen, D. Fantinel, P. Feautrier, T. Fusco, P. Gigan, E. Giro, D. Gisler, L. Gluck, N. Hubin, E. Hugot, M. Jaquet, M. Kasper, F. Madec, Y. Magnard, P. Martinez, D. Maurel, D. Le Mignant, O. Möller-Nilsson, M. Llored, T. Moulin, A. Origné, A. Pavlov, D. Perret, C. Petit, J. Pragt, P. Puget, P. Rabou, J. Ramos, R. Rigal, S. Rochat, R. Roelfsema, G. Rousset, A. Roux, B. Salasnich, J.-F. Sauvage, A. Sevin, C. Soenke, E. Stadler, M. Suarez, L. Weber, F. Wildi, S. Antoniucci, J.-C. Augereau, J.-L. Baudino, W. Brandner, N. Engler, J. Girard, C. Gry, Q. Kral, T. Kopytova, E. Lagadec, J. Milli, C. Moutou, J. Schlieder, J. Szulágyi, C. Thalmann, and Z. Wahhaj. Discovery of a warm, dusty giant planet around HIP 65426. *A&A*, 605:L9, September 2017. doi:10.1051/0004-6361/201731152.

G. Chauvin, R. Gratton, M. Bonnefoy, A.-M. Lagrange, J. de Boer, A. Vigan, H. Beust, C. Lazzoni, A. Boccaletti, R. Galicher, S. Desidera, P. Delorme, M. Keppler, J. Lannier, A.-L. Maire, D. Mesa, N. Meunier, Q. Kral, T. Henning, F. Menard, A. Moor, H. Avenhaus, A. Bazzon, M. Janson, J.-L. Beuzit, T. Bhowmik, M. Bonavita, S. Borgniet, W. Brandner, A. Cheetham, M. Cudel, M. Feldt, C. Fontanive, C. Ginski, J. Hagelberg, P. Janin-Potiron, E. Lagadec, M. Langlois, H. Le Coroller, S. Messina, M. Meyer, D. Mouillet, S. Peretti, C. Perrot, L. Rodet, M. Samland, E. Sissa, J. Olofsson, G. Salter, T. Schmidt, A. Zurlo, J. Milli, R. van Boekel, S. Quanz, P. A. Wilson, P. Feautrier, D. Le Mignant, D. Perret, J. Ramos, and S. Rochat. Investigating the young Solar System analog HD95086. *ArXiv e-prints*, January 2018.

É. Choquet, M. D. Perrin, C. H. Chen, R. Soummer, L. Pueyo, J. B. Hagan, E. Gofas-Salas, A. Rajan, D. A. Golimowski, D. C. Hines, G. Schneider, J. Mazoyer, J.-C. Augereau, J. Debes, C. C. Stark, S. Wolff, M. N'Diaye, and K. Hsiao. First Images of Debris Disks around TWA 7, TWA 25, HD 35650, and HD 377. *ApJL*, 817:L2, January 2016. doi:10.3847/2041-8205/817/1/L2.

T. Currie, S. Daemgen, J. Debes, D. Lafreniere, Y. Itoh, R. Jayawardhana, T. Ratzka, and S. Correia. Direct Imaging and Spectroscopy of a Candidate Companion Below/Near the Deuterium-burning Limit in the Young Binary Star System, ROXs 42B. *ApJL*, 780:L30, January 2014. doi:10.1088/2041-8205/780/2/L30.

R. J. De Rosa, E. L. Nielsen, S. C. Blunt, J. R. Graham, Q. M. Konopacky, C. Marois, L. Pueyo, J. Rameau, D. M. Ryan, J. J. Wang, V. Bailey, A. Chontos, D. C. Fabrycky, K. B. Follette, B. Macintosh, F. Marchis, S. M. Ammons, P. Arriaga, J. K. Chilcote, T. H. Cotten, R. Doyon, G. Duchêne, T. M. Esposito, M. P. Fitzgerald, B. Gerard, S. J. Goodsell, A. Z. Greenbaum, P. Hibon, P. Ingraham, M. Johnson-Groh, P. G. Kalas, D. Lafrenière, J. Maire, S. Metchev, M. A. Millar-Blanchaer, K. M. Morzinski, R. Oppenheimer, R. I. Patel, J. L. Patience, M. D. Perrin, A. Rajan, F. T. Rantakyrö, J.-B. Ruffio, A. C. Schneider, A. Sivaramakrishnan, I. Song, D. Tran, G. Vasisht, K. Ward-Duong, and S. G. Wolff. Astrometric Confirmation and Preliminary Orbital Parameters of the Young Exoplanet 51 Eridani b with the Gemini Planet Imager. *ApJL*, 814:L3, November 2015. doi:10.1088/2041-8205/814/1/L3.

V. D'Orazi, S. Desidera, R. G. Gratton, A. F. Lanza, S. Messina, S. M. Andrievsky, S. Korotin, S. Benatti, M. Bonnefoy, E. Covino, and M. Janson. A critical reassessment of the fundamental properties of GJ 504: chemical composition and age. *A&A*, 598:A19, February 2017. doi:10.1051/0004-6361/201629283.

K. Fuhrmann and R. Chini. On the age of Gliese 504. *ApJ*, 806:163, June 2015. doi:10.1088/0004-637X/806/2/163.

B. Gauza, V. J. S. Béjar, A. Pérez-Garrido, M. Rosa Zapatero Osorio, N. Lodieu, R. Rebolo, E. Pallé, and G. Nowak. Discovery of a Young Planetary Mass Companion to the Nearby M Dwarf VHS J125601.92-125723.9. *ApJ*, 804:96, May 2015. doi:10.1088/0004-637X/804/2/96.

A. Glasse, G. H. Rieke, E. Bauwens, M. García-Marín, M. E. Ressler, S. Rost, T. V. Tikkanen, B. Vandenbussche, and G. S. Wright. The Mid-Infrared Instrument for the James Webb Space Telescope, IX: Predicted Sensitivity. *PASP*, 127:686, July 2015. doi:10.1086/682259.

P. M. Hinz. Detection of Debris Disks and Wide Orbit Planets with the LBTI. In T. Usuda, M. Tamura, and M. Ishii, editors, *American Institute of Physics Conference Series*, volume 1158 of *American Institute of Physics Conference Series*, pages 313–317, August 2009. doi:10.1063/1.3215875.

P. G. J. Irwin, N. A. Teanby, R. de Kok, L. N. Fletcher, C. J. A. Howett, C. C. C. Tsang, C. F. Wilson, S. B. Calcutt, C. A. Nixon, and P. D. Parrish. The NEMESIS planetary atmosphere radiative transfer and retrieval tool. *JQSRT*, 109:1136–1150, April 2008. doi:10.1016/j.jqsrt.2007.11.006.

S. Kendrew, S. Scheithauer, P. Bouchet, J. Amiaux, R. Azzollini, J. Bouwman, C. H. Chen, D. Dubreuil, S. Fischer, A. Glasse, T. P. Greene, P.-O. Lagage, F. Lahuis, S. Ronayette, D. Wright, and G. S. Wright. The Mid-Infrared Instrument for the James Webb Space Telescope, IV: The Low-Resolution Spectrometer. *PASP*, 127:623, July 2015. doi:10.1086/682255.

M. Kuzuhara, M. Tamura, T. Kudo, M. Janson, R. Kandori, T. D. Brandt, C. Thalmann, D. Spiegel, B. Biller, J. Carson, Y. Hori, R. Suzuki, A. Burrows, T. Henning, E. L. Turner, M. W. McElwain, A. Moro-Martín, T. Suenaga, Y. H. Takahashi, J. Kwon, P. Lucas, L. Abe, W. Brandner, S. Egner, M. Feldt, H. Fujiwara, M. Goto, C. A. Grady, O. Guyon, J. Hashimoto, Y. Hayano, M. Hayashi, S. S. Hayashi, K. W. Hodapp, M. Ishii, M. Iye, G. R. Knapp, T. Matsuo, S. Mayama, S. Miyama, J.-I. Morino, J. Nishikawa, T. Nishimura, T. Kotani, N. Kusakabe, T.-S. Pyo, E. Serabyn, H. Suto, M. Takami, N. Takato, H. Terada, D. Tomono, M. Watanabe, J. P. Wisniewski, T. Yamada, H. Takami, and T. Usuda. Direct Imaging of a Cold Jovian Exoplanet in Orbit around the Sun-like Star GJ 504. *ApJ*, 774:11, September 2013. doi:10.1088/0004-637X/774/1/11.

D. Lafrenière, C. Marois, R. Doyon, D. Nadeau, and É. Artigau. A New Algorithm for Point-Spread Function Subtraction in High-Contrast Imaging: A Demonstration with Angular Differential Imaging. *ApJ*, 660:770–780, May 2007. doi:10.1086/513180.

A.-M. Lagrange, D. Gratadour, G. Chauvin, T. Fusco, D. Ehrenreich, D. Mouillet, G. Rousset, D. Rouan, F. Allard, É. Gendron, J. Charton, L. Mugnier, P. Rabou, J. Montri, and F. Lacombe. A probable giant planet imaged in the β Pictoris disk. VLT/NaCo deep L'-band imaging. *A&A*, 493:L21–L25, January 2009. doi:10.1051/0004-6361:200811325.

C.-P. Lajoie, R. Soummer, D. C. Hines, and G. H. Rieke. Simulations of JWST MIRI 4QPM coronagraphs operations and performances. In *Space Telescopes and Instrumentation 2014: Optical, Infrared, and Millimeter Wave*, volume 9143 of *Proc. SPIE*, page 91433R, August 2014. doi:10.1117/12.2056284.

C.-P. Lajoie, R. Soummer, L. Pueyo, D. C. Hines, E. P. Nelan, M. Perrin, M. Clampin, and J. C. Isaacs. Small-grid dithers for the JWST coronagraphs. In *Space Telescopes and Instrumentation 2016: Optical, Infrared, and Millimeter Wave*, volume 9904 of *Proc. SPIE*, page 99045K, July 2016. doi:10.1117/12.2233032.

M. R. Line, A. S. Wolf, X. Zhang, H. Knutson, J. A. Kammer, E. Ellison, P. Deroo, D. Crisp, and Y. L. Yung. A Systematic Retrieval Analysis of Secondary Eclipse Spectra. I. A Comparison of Atmospheric Retrieval Techniques. *ApJ*, 775:137, October 2013. doi:10.1088/0004-637X/775/2/137.

B. Macintosh, J. R. Graham, P. Ingraham, Q. Konopacky, C. Marois, M. Perrin, L. Poyneer, B. Bauman, T. Barman, A. S. Burrows, A. Cardwell, J. Chilcote, R. J. De Rosa, D. Dillon, R. Doyon, J. Dunn, D. Erikson, M. P. Fitzgerald, D. Gavel, S. Goodsell, M. Hartung, P. Hibon, P. Kalas, J. Larkin, J. Maire, F. Marchis, M. S. Marley, J. McBride, M. Millar-Blanchaer, K. Morzinski, A. Norton, B. R. Oppenheimer, D. Palmer, J. Patience, L. Pueyo, F. Rantakyro, N. Sadakuni, L. Saddlemyer, D. Savransky, A. Serio, R. Soummer, A. Sivaramakrishnan, I. Song, S. Thomas, J. K. Wallace, S. Wiktorowicz, and S. Wolff. First light of the Gemini Planet Imager. *Proceedings of the National Academy of Science*, 111:12661–12666, September 2014. doi:10.1073/pnas.1304215111.

B. Macintosh, J. R. Graham, T. Barman, R. J. De Rosa, Q. Konopacky, M. S. Marley, C. Marois, E. L. Nielsen, L. Pueyo, A. Rajan, J. Rameau, D. Saumon, J. J. Wang, J. Patience, M. Ammons, P. Arriaga, E. Artigau, S. Beckwith, J. Brewster, S. Bruzzone, J. Bulger, B. Burningham, A. S. Burrows, C. Chen, E. Chiang, J. K. Chilcote, R. I. Dawson, R. Dong, R. Doyon, Z. H. Draper, G. Duchêne, T. M. Esposito, D. Fabrycky, M. P. Fitzgerald, K. B. Follette, J. J. Fortney, B. Gerard, S. Goodsell, A. Z. Greenbaum, P. Hibon, S. Hinkley, T. H. Cotten, L.-W. Hung, P. Ingraham, M. Johnson-Groh, P. Kalas, D. Lafreniere, J. E. Larkin, J. Lee, M. Line, D. Long, J. Maire, F. Marchis, B. C. Matthews, C. E. Max, S. Metchev, M. A. Millar-Blanchaer, T. Mittal, C. V. Morley, K. M. Morzinski, R. Murray-Clay, R. Oppenheimer, D. W. Palmer, R. Patel, M. D. Perrin, L. A. Poyneer, R. R. Rafikov, F. T. Rantakyrö, E. L. Rice, P. Rojo, A. R. Rudy, J.-B. Ruffio, M. T. Ruiz, N. Sadakuni, L. Saddlemyer, M. Salama, D. Savransky, A. C. Schneider, A. Sivaramakrishnan, I. Song, R. Soummer, S. Thomas, G. Vasisht, J. K. Wallace, K. Ward-Duong, S. J. Wiktorowicz, S. G. Wolff, and B. Zuckerman. Discovery and spectroscopy of the young jovian planet 51 Eri b with the Gemini Planet Imager. *Science*, 350:64–67, October 2015. doi:10.1126/science.aac5891.

C. Marois, B. Macintosh, T. Barman, B. Zuckerman, I. Song, J. Patience, D. Lafrenière, and R. Doyon. Direct Imaging of Multiple Planets Orbiting the Star HR 8799. *Science*, 322:1348, November 2008. doi:10.1126/science.1166585.

C. Marois, B. Zuckerman, Q. M. Konopacky, B. Macintosh, and T. Barman. Images of a fourth planet orbiting HR 8799. *Nature*, 468: 1080–1083, December 2010. doi:10.1038/nature09684.

I. S. McLean and D. Sprayberry. Instrumentation at the Keck observatory. In M. Iye and A. F. M. Moorwood, editors, *Instrument Design and Performance for Optical/Infrared Ground-based Telescopes*, volume 4841 of *Proc. SPIE*, pages 1–6, March 2003. doi:10.1117/12.461785.

D. Mesa, A. Zurlo, J. Milli, R. Gratton, S. Desidera, M. Langlois, A. Vigan, M. Bonavita, J. Antichi, H. Avenhaus, A. Baruffolo, B. Biller, A. Boccaletti, P. Bruno, E. Cascone, G. Chauvin, R. U. Claudi, V. De Caprio, D. Fantinel, G. Farisato, J. Girard, E. Giro, J. Hagelberg, S. Incorvaia, M. Janson, Q. Kral, E. Lagadec, A.-M. Lagrange, L. Lessio, M. Meyer, S. Peretti, C. Perrot, B. Salasnich, J. Schlieder, H.-M. Schmid, S. Scuderi, E. Sissa, C. Thalmann, and M. Turatto. Upper limits for mass and radius of objects around Proxima Cen from SPHERE/VLT. *MNRAS*, 466: L118–L122, March 2017. doi:10.1093/mnrasl/slw241.

J. Rameau, G. Chauvin, A.-M. Lagrange, A. Boccaletti, S. P. Quanz, M. Bonnefoy, J. H. Girard, P. Delorme, S. Desidera, H. Klahr, C. Mordasini, C. Dumas, and M. Bonavita. Discovery of a Probable 4-5 Jupiter-mass Exoplanet to HD 95086 by Direct Imaging. *ApJL*, 772:L15, August 2013a. doi:10.1088/2041-8205/772/2/L15.

J. Rameau, G. Chauvin, A.-M. Lagrange, T. Meshkat, A. Boccaletti, S. P. Quanz, T. Currie, D. Mawet, J. H. Girard, M. Bonnefoy, and M. Kenworthy. Confirmation of the Planet around HD 95086 by Direct Imaging. *ApJL*, 779: L26, December 2013b. doi:10.1088/2041-8205/779/2/L26.

M. E. Ressler, K. G. Sukhatme, B. R. Franklin, J. C. Mahoney, M. P. Thelen, P. Bouchet, J. W. Colbert, M. Cracraft, D. Dicken, R. Gastaud, G. B. Goodson, P. Eccleston, V. Moreau, G. H. Rieke, and A. Schneider. The Mid-Infrared Instrument for the James Webb Space Telescope, VIII: The MIRI Focal Plane System. *PASP*, 127:675, July 2015. doi:10.1086/682258.

G. H. Rieke, G. S. Wright, T. Böker, J. Bouwman, L. Colina, A. Glasse, K. D. Gordon, T. P. Greene, M. Güdel, T. Henning, K. Justtanont, P.-O. Lagage, M. E. Meixner, H.-U. Nørgaard-Nielsen, T. P. Ray, M. E. Ressler, E. F. van Dishoeck, and C. Waelkens. The Mid-Infrared Instrument for the James Webb Space Telescope, I: Introduction. *PASP*, 127: 584, July 2015. doi:10.1086/682252.

M. Rocchetto, I. P. Waldmann, O. Venot, P.-O. Lagage, and G. Tinetti. Exploring Biases of Atmospheric Retrievals in Simulated JWST Transmission Spectra of Hot Jupiters. *ApJ*, 833:120, December 2016. doi:10.3847/1538-4357/833/1/120.

D. Rouan, P. Riaud, A. Boccaletti, Y. Clénet, and A. Labeyrie. The Four-Quadrant Phase-Mask Coronagraph. I. Principle. *PASP*, 112: 1479–1486, November 2000. doi:10.1086/317707.

R. Soummer, L. Pueyo, and J. Larkin. Detection and Characterization of Exoplanets and Disks Using Projections on Karhunen-Loève Eigenimages. *ApJL*, 755:L28, August 2012. doi:10.1088/2041-8205/755/2/L28.

R. Soummer, C.-P. Lajoie, L. Pueyo, D. C. Hines, J. C. Isaacs, E. P. Nelan, M. Clampin, and M. Perrin. Small-grid dithering strategy for improved coronagraphic performance with JWST. In *Space Telescopes and Instrumentation 2014: Optical, Infrared, and Millimeter Wave*, volume 9143 of *Proc. SPIE*, page 91433V, August 2014. doi:10.1117/12.2057190.

J. M. Stone, A. J. Skemer, K. M. Kratter, T. J. Dupuy, L. M. Close, J. A. Eisner, J. J. Fortney, P. M. Hinz, J. R. Males, C. V. Morley, K. M. Morzinski, and K. Ward-Duong. Adaptive Optics imaging of VHS 1256-1257: A Low Mass Companion to a Brown Dwarf Binary System. *ApJL*, 818:L12, February 2016. doi:10.3847/2041-8205/818/1/L12.

A. Vigan, C. Gry, G. Salter, D. Mesa, D. Homeier, C. Moutou, and F. Allard. High-contrast imaging of Sirius A with VLT/SPHERE: looking for giant planets down to one astronomical unit. *MNRAS*, 454:129–143, November 2015. doi:10.1093/mnras/stv1928.

I. P. Waldmann, G. Tinetti, M. Rocchetto, E. J. Barton, S. N. Yurchenko, and J. Tennyson. Tau-REx I: A Next Generation Retrieval Code for Exoplanetary Atmospheres. *ApJ*, 802:107, April 2015. doi:10.1088/0004-637X/802/2/107.

M. Wells, J.-W. Pel, A. Glasse, G. S. Wright, G. Aitink-Kroes, R. Azzollini, S. Beard, B. R. Brandl, A. Gallie, V. C. Geers, A. M. Glauser, P. Hastings, T. Henning, R. Jager, K. Justtanont, B. Kruizinga, F. Lahuis, D. Lee, I. Martinez-Delgado, J. R. Martínez-Galarza, M. Meijers, J. E. Morrison, F. Müller, T. Nakos, B. O'Sullivan, A. Oudenhuysen, P. Parr-Burman, E. Pauwels, R.-R. Rohloff, E. Schmalzl, J. Sykes, M. P. Thelen, E. F. van Dishoeck, B. Vandenbussche, L. B. Venema, H. Visser, L. B. F. M. Waters, and D. Wright. The Mid-Infrared Instrument for the James Webb Space Telescope, VI: The Medium Resolution Spectrometer. *PASP*, 127:646, July 2015. doi:10.1086/682281.

E. L. Wright, P. R. M. Eisenhardt, A. K. Mainzer, M. E. Ressler, R. M. Cutri, T. Jarrett, J. D. Kirkpatrick, D. Padgett, R. S. McMillan, M. Skrutskie, S. A. Stanford, M. Cohen, R. G. Walker, J. C. Mather, D. Leisawitz, T. N. Gautier, III, I. McLean, D. Benford, C. J. Lonsdale, A. Blain, B. Mendez, W. R. Irace, V. Duval, F. Liu, D. Royer, I. Heinrichsen, J. Howard, M. Shannon, M. Kendall, A. L. Walsh, M. Larsen, J. G. Cardon, S. Schick, M. Schwalm, M. Abid, B. Fabinsky, L. Naes, and C.-W. Tsai. The Wide-field Infrared Survey Explorer (WISE): Mission Description and Initial On-orbit Performance. *AJ*, 140:1868-1881, December 2010. doi:10.1088/0004-6256/140/6/1868.

G. S. Wright, D. Wright, G. B. Goodson, G. H. Rieke, G. Aitink-Kroes, J. Amiaux, A. Aricha-Yanguas, R. Azzollini, K. Banks, D. Barrado-Navascues, T. Belenguer-Davila, J. A. D. L. Bloemmart, P. Bouchet, B. R. Brandl, L. Colina, Ö. Detre, E. Diaz-Catala, P. Eccleston, S. D. Friedman, M. García-Marín, M. Güdel, A. Glasse, A. M. Glauser, T. P. Greene, U. Groezinger, T. Grundy, P. Hastings, T. Henning, R. Hofferbert, F. Hunter, N. C. Jessen, K. Justtanont, A. R. Karnik, M. A. Khorrami, O. Krause, A. Labiano, P.-O. Lagage, U. Langer, D. Lemke, T. Lim, J. Lorenzo-Alvarez, E. Mazy, N. McGowan, M. E. Meixner, N. Morris, J. E. Morrison, F. Müller, H.-U. N. rgaard-Nielson, G. Olofsson, B. O'Sullivan, J.-W. Pel, K. Penanen, M. B. Petach, J. P. Pye, T. P. Ray, E. Renotte, I. Renouf, M. E. Ressler, P. Samara-Ratna, S. Scheithauer, A. Schneider, B. Shaughnessy, T. Stevenson, K. Sukhatme, B. Swinyard, J. Sykes, J. Thatcher, T. Tikkanen, E. F. van Dishoeck, C. Waelkens, H. Walker, M. Wells, and A. Zhender. The Mid-Infrared Instrument for the James Webb Space Telescope, II: Design and Build. *PASP*, 127:595, July 2015. doi:10.1086/682253.

APPENDIX

A. PLANETARY CONTRAST

.

Table 9. Planetary contrast of the coronagraphic targets measured in the three 4QPM filters using Exo-REM atmospheric model. The equilibrium and non equilibrium cases are represented by the "eq" and "neq" strings, respectively.

Planet		F1065C	F1140C	F1550C
β Pictoris b	eq	7.19	7.17	7.23
	neq	7.22	7.17	7.23
51 Eri b	eq	11.32	10.29	10.16
	neq	10.66	10.11	10.07
GJ 504 b	eq	10.60	9.01	8.91
	neq	9.43	8.64	8.83
HD 95086 b	eq	9.59	9.38	9.38
	neq	9.87	9.59	9.58
2M1207 b	eq	2.19	2.12	2.0
	neq	3.88	3.88	3.88
ROXs42 b	eq	1.91	1.98	2.02
	neq	1.91	1.98	2.02
HIP 65426 b	eq	8.05	7.88	7.95
	neq	8.32	8.08	8.09
HR 8799 b	eq	7.96	7.86	7.776
	neq	8.70	8.43	8.19
HR 8799 c	eq	7.78	7.69	7.6
	neq	8.02	7.87	7.71
HR 8799 d	eq	7.93	7.82	7.78
	neq	8.19	8.05	7.88
HR 8799 e	eq	8.33	8.24	8.15
	neq	8.54	8.41	8.19

B. CONTRAST CURVES

B.1. *F1065C*

Table 10. F1065C 1 σ contrast curves as a function of the angular distance (Ang.Dist) for observational cases k_A, k_B, k_C, k_D.

Ang. Dist.[″]	k_A	k_B	k_C	k_D
0.11	8.7e-06	1.1e-04	1.5e-04	4.5e-04
0.22	8.8e-06	1.0e-04	1.3e-04	4.0e-04
0.33	8.8e-06	1.0e-04	1.3e-04	3.9e-04
0.44	7.9e-06	9.3e-05	1.1e-04	3.5e-04
0.55	6.3e-06	7.5e-05	8.7e-05	2.7e-04
0.66	4.6e-06	5.6e-05	6.7e-05	2.1e-04
0.77	2.7e-06	3.4e-05	4.6e-05	1.4e-04
0.88	2.6e-06	3.3e-05	4.6e-05	1.4e-04
0.99	2.2e-06	2.8e-05	4.0e-05	1.2e-04
1.10	1.9e-06	2.3e-05	3.3e-05	1.0e-04
1.21	1.6e-06	1.9e-05	2.6e-05	8.0e-05
1.32	1.4e-06	1.7e-05	2.4e-05	7.3e-05
1.43	1.3e-06	1.6e-05	2.3e-05	7.0e-05
1.54	1.0e-06	1.2e-05	1.6e-05	5.0e-05
1.65	8.6e-07	1.0e-05	1.3e-05	4.1e-05
1.76	8.0e-07	9.8e-06	1.2e-05	3.7e-05
1.87	6.8e-07	8.3e-06	1.0e-05	3.2e-05
1.98	5.6e-07	6.9e-06	8.6e-06	2.6e-05
2.09	5.0e-07	6.2e-06	8.0e-06	2.5e-05
2.20	4.6e-07	5.7e-06	7.6e-06	2.3e-05
2.31	4.0e-07	4.9e-06	6.6e-06	2.0e-05
2.42	3.5e-07	4.2e-06	5.9e-06	1.8e-05
2.53	4.0e-07	4.8e-06	6.5e-06	2.0e-05
2.64	3.9e-07	4.7e-06	6.4e-06	2.0e-05
2.75	3.6e-07	4.3e-06	5.9e-06	1.8e-05
2.86	3.4e-07	4.2e-06	6.1e-06	1.9e-05
2.97	3.0e-07	3.6e-06	5.5e-06	1.7e-05
3.08	2.7e-07	3.4e-06	5.2e-06	1.6e-05
3.19	2.3e-07	2.8e-06	4.4e-06	1.3e-05
3.30	1.8e-07	2.3e-06	3.7e-06	1.1e-05
3.41	1.9e-07	2.3e-06	3.7e-06	1.1e-05
3.52	1.9e-07	2.3e-06	3.9e-06	1.2e-05

Table 10. continued.

Ang.Dist.[″]	k_A	k_B	k_C	k_D
3.63	1.9e-07	2.3e-06	3.9e-06	1.2e-05
3.74	1.7e-07	2.1e-06	3.6e-06	1.1e-05
3.85	1.7e-07	2.0e-06	3.3e-06	1.0e-05
3.96	1.7e-07	2.2e-06	3.1e-06	9.5e-06
4.07	1.6e-07	1.9e-06	2.7e-06	8.3e-06
4.18	1.6e-07	2.0e-06	2.6e-06	8.0e-06
4.29	1.4e-07	1.7e-06	2.3e-06	7.0e-06
4.40	1.3e-07	1.5e-06	2.2e-06	6.7e-06
4.51	1.1e-07	1.3e-06	1.9e-06	6.0e-06
4.62	1.0e-07	1.2e-06	1.8e-06	5.6e-06
4.73	9.2e-08	1.1e-06	1.7e-06	5.1e-06
4.84	8.2e-08	9.5e-07	1.5e-06	4.7e-06
4.95	8.3e-08	9.8e-07	1.5e-06	4.5e-06
5.06	7.9e-08	9.5e-07	1.4e-06	4.2e-06
5.17	7.5e-08	9.1e-07	1.3e-06	3.9e-06
5.28	6.7e-08	8.2e-07	1.1e-06	3.4e-06
5.39	6.2e-08	7.5e-07	1.0e-06	3.2e-06
5.50	5.5e-08	6.7e-07	9.7e-07	3.0e-06
5.61	4.4e-08	5.3e-07	8.3e-07	2.5e-06
5.72	4.7e-08	5.7e-07	8.8e-07	2.7e-06
5.83	4.7e-08	5.7e-07	8.5e-07	2.6e-06
5.94	4.6e-08	5.6e-07	8.4e-07	2.6e-06
6.05	4.8e-08	5.7e-07	8.6e-07	2.7e-06
6.16	4.3e-08	5.1e-07	8.4e-07	2.6e-06
6.27	4.3e-08	5.2e-07	8.3e-07	2.6e-06
6.38	4.0e-08	4.9e-07	8.1e-07	2.5e-06
6.49	3.7e-08	4.6e-07	7.9e-07	2.4e-06
6.60	3.4e-08	4.1e-07	7.2e-07	2.2e-06
6.71	3.1e-08	3.8e-07	6.5e-07	2.0e-06
6.82	3.0e-08	3.7e-07	6.0e-07	1.8e-06
6.93	2.7e-08	3.3e-07	5.4e-07	1.7e-06
7.04	2.7e-08	3.3e-07	5.2e-07	1.6e-06
7.15	2.5e-08	3.0e-07	4.7e-07	1.4e-06
7.26	2.4e-08	2.9e-07	4.5e-07	1.4e-06
7.37	2.4e-08	2.9e-07	4.5e-07	1.4e-06
7.48	2.3e-08	2.7e-07	4.3e-07	1.3e-06
7.59	2.4e-08	2.7e-07	4.3e-07	1.3e-06

Table 10. continued.

Ang.Dist.[″]	k_A	k_B	k_C	k_D
7.70	2.5e-08	2.9e-07	4.5e-07	1.4e-06
7.81	2.5e-08	2.8e-07	4.6e-07	1.4e-06
7.92	2.7e-08	2.9e-07	4.8e-07	1.5e-06
8.03	2.6e-08	2.8e-07	4.8e-07	1.5e-06
8.14	2.5e-08	2.8e-07	4.8e-07	1.5e-06
8.25	2.3e-08	2.6e-07	4.5e-07	1.4e-06
8.36	2.0e-08	2.2e-07	4.1e-07	1.3e-06
8.47	1.7e-08	2.0e-07	3.6e-07	1.1e-06
8.58	1.5e-08	1.8e-07	3.1e-07	9.5e-07
8.69	1.4e-08	1.7e-07	2.8e-07	8.6e-07
8.80	1.4e-08	1.7e-07	2.7e-07	8.2e-07
8.91	1.3e-08	1.6e-07	2.6e-07	7.9e-07
9.02	1.4e-08	1.6e-07	2.7e-07	8.2e-07
9.13	1.6e-08	1.8e-07	3.0e-07	9.1e-07
9.24	1.6e-08	1.9e-07	3.1e-07	9.6e-07
9.35	1.6e-08	1.8e-07	3.2e-07	9.7e-07
9.46	1.6e-08	1.7e-07	3.2e-07	9.9e-07
9.57	1.6e-08	1.7e-07	3.1e-07	9.7e-07
9.68	1.4e-08	1.5e-07	3.0e-07	9.3e-07
9.79	1.3e-08	1.4e-07	2.8e-07	8.7e-07
9.90	1.2e-08	1.3e-07	2.6e-07	8.1e-07
10.01	1.1e-08	1.2e-07	2.4e-07	7.4e-07
10.12	1.0e-08	1.1e-07	2.2e-07	6.9e-07
10.23	1.0e-08	1.1e-07	2.1e-07	6.5e-07
10.34	9.5e-09	1.1e-07	2.0e-07	6.1e-07
10.45	9.3e-09	1.1e-07	1.9e-07	5.8e-07
10.56	9.0e-09	1.0e-07	1.8e-07	5.5e-07
10.67	8.2e-09	9.2e-08	1.7e-07	5.2e-07
10.78	8.6e-09	9.7e-08	1.7e-07	5.2e-07
10.89	8.4e-09	9.1e-08	1.6e-07	5.0e-07
11.00	9.1e-09	9.8e-08	1.7e-07	5.3e-07

B.2. *F1140C*

Table 11. F1140C 1 σ contrast curves as a function of the angular distance (Ang.Dist) for observational cases k_A, k_B, k_C, k_D.

Ang. Dist.[″]	k_A	k_B	k_C	k_D
0.11	9.9e-06	1.2e-04	1.7e-04	5.1e-04
0.22	8.8e-06	1.0e-04	1.4e-04	4.2e-04
0.33	8.6e-06	1.0e-04	1.3e-04	4.0e-04
0.44	7.4e-06	8.8e-05	1.1e-04	3.3e-04
0.55	5.0e-06	6.1e-05	7.4e-05	2.3e-04
0.66	4.0e-06	4.9e-05	6.3e-05	2.0e-04
0.77	3.2e-06	3.9e-05	5.3e-05	1.7e-04
0.88	3.0e-06	3.8e-05	5.1e-05	1.6e-04
0.99	2.2e-06	2.7e-05	3.8e-05	1.2e-04
1.10	1.8e-06	2.2e-05	3.0e-05	9.4e-05
1.21	1.7e-06	2.0e-05	2.7e-05	8.4e-05
1.32	1.6e-06	2.0e-05	2.7e-05	8.3e-05
1.43	1.5e-06	1.8e-05	2.5e-05	7.7e-05
1.54	1.1e-06	1.3e-05	1.9e-05	5.7e-05
1.65	9.7e-07	1.2e-05	1.6e-05	5.1e-05
1.76	8.8e-07	1.1e-05	1.5e-05	4.5e-05
1.87	7.4e-07	9.0e-06	1.2e-05	3.7e-05
1.98	6.4e-07	7.8e-06	1.1e-05	3.4e-05
2.09	5.7e-07	7.0e-06	9.7e-06	3.0e-05
2.20	5.1e-07	6.3e-06	8.6e-06	2.7e-05
2.31	4.4e-07	5.4e-06	7.6e-06	2.4e-05
2.42	3.8e-07	4.7e-06	6.6e-06	2.1e-05
2.53	3.8e-07	4.6e-06	6.4e-06	2.0e-05
2.64	3.5e-07	4.2e-06	6.0e-06	1.9e-05
2.75	3.4e-07	4.1e-06	6.0e-06	1.8e-05
2.86	3.6e-07	4.3e-06	6.2e-06	1.9e-05
2.97	3.2e-07	3.9e-06	5.7e-06	1.8e-05
3.08	3.4e-07	4.2e-06	6.1e-06	1.9e-05
3.19	3.0e-07	3.6e-06	5.4e-06	1.7e-05
3.30	2.2e-07	2.7e-06	4.2e-06	1.3e-05
3.41	2.1e-07	2.6e-06	4.0e-06	1.2e-05
3.52	2.1e-07	2.5e-06	3.9e-06	1.2e-05
3.63	2.0e-07	2.4e-06	3.8e-06	1.2e-05

Table 11. continued.

Ang.Dist.[″]	k_A	k_B	k_C	k_D
3.74	1.8e-07	2.3e-06	3.6e-06	1.1e-05
3.85	1.8e-07	2.2e-06	3.5e-06	1.0e-05
3.96	1.8e-07	2.1e-06	3.5e-06	1.1e-05
4.07	1.6e-07	2.0e-06	3.2e-06	9.7e-06
4.18	1.8e-07	2.3e-06	3.3e-06	1.0e-05
4.29	1.6e-07	1.9e-06	2.8e-06	8.7e-06
4.40	1.7e-07	2.1e-06	2.9e-06	9.0e-06
4.51	1.5e-07	1.8e-06	2.6e-06	8.1e-06
4.62	1.3e-07	1.5e-06	2.3e-06	7.1e-06
4.73	1.1e-07	1.4e-06	2.1e-06	6.4e-06
4.84	1.0e-07	1.2e-06	1.9e-06	5.8e-06
4.95	9.7e-08	1.1e-06	1.8e-06	5.5e-06
5.06	9.3e-08	1.1e-06	1.7e-06	5.3e-06
5.17	9.0e-08	1.1e-06	1.6e-06	5.0e-06
5.28	8.3e-08	9.8e-07	1.5e-06	4.6e-06
5.39	8.0e-08	9.5e-07	1.4e-06	4.4e-06
5.50	7.4e-08	9.0e-07	1.3e-06	4.0e-06
5.61	6.4e-08	7.8e-07	1.1e-06	3.5e-06
5.72	6.7e-08	8.1e-07	1.2e-06	3.6e-06
5.83	5.9e-08	7.1e-07	1.0e-06	3.3e-06
5.94	5.2e-08	6.3e-07	9.5e-07	3.0e-06
6.05	4.8e-08	5.8e-07	8.8e-07	2.7e-06
6.16	4.0e-08	4.8e-07	7.6e-07	2.4e-06
6.27	4.7e-08	5.6e-07	8.5e-07	2.7e-06
6.38	4.8e-08	5.7e-07	8.8e-07	2.7e-06
6.49	4.5e-08	5.3e-07	8.6e-07	2.7e-06
6.60	4.6e-08	5.5e-07	8.8e-07	2.7e-06
6.71	4.3e-08	5.2e-07	8.7e-07	2.7e-06
6.82	4.0e-08	4.8e-07	8.3e-07	2.6e-06
6.93	3.7e-08	4.6e-07	8.1e-07	2.5e-06
7.04	3.6e-08	4.4e-07	7.8e-07	2.4e-06
7.15	3.3e-08	4.0e-07	7.1e-07	2.2e-06
7.26	3.1e-08	3.7e-07	6.4e-07	2.0e-06
7.37	2.9e-08	3.4e-07	5.5e-07	1.7e-06
7.48	2.7e-08	3.2e-07	5.0e-07	1.5e-06
7.59	2.5e-08	3.0e-07	4.6e-07	1.4e-06
7.70	2.5e-08	3.0e-07	4.7e-07	1.5e-06

Table 11. continued.

Ang.Dist.[″]	k_A	k_B	k_C	k_D
7.81	2.2e-08	2.6e-07	4.3e-07	1.3e-06
7.92	2.4e-08	2.8e-07	4.5e-07	1.4e-06
8.03	2.2e-08	2.5e-07	4.2e-07	1.3e-06
8.14	2.4e-08	2.8e-07	4.4e-07	1.4e-06
8.25	2.5e-08	2.8e-07	4.4e-07	1.4e-06
8.36	2.5e-08	2.7e-07	4.5e-07	1.4e-06
8.47	2.6e-08	2.9e-07	4.9e-07	1.5e-06
8.58	2.7e-08	2.9e-07	5.1e-07	1.6e-06
8.69	2.6e-08	2.8e-07	5.0e-07	1.6e-06
8.80	2.4e-08	2.7e-07	5.0e-07	1.5e-06
8.91	2.1e-08	2.4e-07	4.5e-07	1.4e-06
9.02	1.8e-08	2.1e-07	3.9e-07	1.2e-06
9.13	1.6e-08	1.9e-07	3.2e-07	1.0e-06
9.24	1.4e-08	1.7e-07	2.7e-07	8.5e-07
9.35	1.2e-08	1.5e-07	2.4e-07	7.5e-07
9.46	1.2e-08	1.4e-07	2.4e-07	7.3e-07
9.57	1.3e-08	1.6e-07	2.5e-07	7.8e-07
9.68	1.3e-08	1.5e-07	2.5e-07	7.9e-07
9.79	1.5e-08	1.7e-07	2.8e-07	8.8e-07
9.90	1.6e-08	1.8e-07	3.0e-07	9.4e-07
10.01	1.7e-08	1.9e-07	3.4e-07	1.1e-06
10.12	1.7e-08	1.8e-07	3.4e-07	1.1e-06
10.23	1.7e-08	1.8e-07	3.5e-07	1.1e-06
10.34	1.6e-08	1.7e-07	3.3e-07	1.0e-06
10.45	1.4e-08	1.5e-07	3.1e-07	9.7e-07
10.56	1.2e-08	1.3e-07	2.7e-07	8.3e-07
10.67	1.1e-08	1.2e-07	2.5e-07	7.9e-07
10.78	1.0e-08	1.2e-07	2.3e-07	7.3e-07
10.89	9.1e-09	1.0e-07	2.1e-07	6.7e-07
11.00	1.0e-08	1.2e-07	2.1e-07	6.5e-07

B.3. *F1550C*

Table 12. F1140C 1 σ contrast curves as a function of the angular distance (Ang.Dist) for observational cases k_A, k_B, k_C, k_D.

Ang. Dist.[$''$]	k_A	k_B	k_C	k_D
0.11	2.8e-06	3.2e-05	4.8e-05	1.5e-04
0.22	2.7e-06	3.1e-05	4.7e-05	1.4e-04
0.33	2.7e-06	3.0e-05	4.2e-05	1.3e-04
0.44	2.6e-06	3.0e-05	4.0e-05	1.2e-04
0.55	2.3e-06	2.7e-05	3.4e-05	1.1e-04
0.66	1.9e-06	2.3e-05	2.8e-05	8.6e-05
0.77	1.7e-06	2.1e-05	2.5e-05	7.8e-05
0.88	1.3e-06	1.7e-05	2.2e-05	6.9e-05
0.99	1.1e-06	1.3e-05	2.0e-05	6.3e-05
1.10	7.6e-07	9.4e-06	1.6e-05	4.9e-05
1.21	6.8e-07	8.6e-06	1.4e-05	4.5e-05
1.32	6.3e-07	8.0e-06	1.3e-05	4.1e-05
1.43	5.2e-07	6.5e-06	1.0e-05	3.2e-05
1.54	5.0e-07	6.2e-06	8.9e-06	2.7e-05
1.65	5.1e-07	6.2e-06	8.4e-06	2.6e-05
1.76	5.0e-07	6.1e-06	8.2e-06	2.5e-05
1.87	4.9e-07	5.9e-06	7.8e-06	2.4e-05
1.98	4.4e-07	5.3e-06	7.0e-06	2.1e-05
2.09	4.2e-07	5.0e-06	6.9e-06	2.1e-05
2.20	3.7e-07	4.4e-06	6.2e-06	1.9e-05
2.31	3.3e-07	4.0e-06	5.4e-06	1.6e-05
2.42	2.9e-07	3.5e-06	4.4e-06	1.3e-05
2.53	2.6e-07	3.2e-06	3.9e-06	1.2e-05
2.64	2.3e-07	2.8e-06	3.6e-06	1.1e-05
2.75	2.0e-07	2.5e-06	3.1e-06	9.7e-06
2.86	1.8e-07	2.2e-06	2.7e-06	8.2e-06
2.97	1.6e-07	2.0e-06	2.5e-06	7.6e-06
3.08	1.5e-07	1.8e-06	2.4e-06	7.5e-06
3.19	1.2e-07	1.5e-06	2.2e-06	6.8e-06
3.30	1.2e-07	1.4e-06	2.2e-06	6.7e-06
3.41	1.2e-07	1.5e-06	2.4e-06	7.3e-06
3.52	1.2e-07	1.4e-06	2.3e-06	6.9e-06
3.63	1.2e-07	1.4e-06	2.4e-06	7.3e-06

Table 12. continued.

Ang.Dist.[″]	k_A	k_B	k_C	k_D
3.74	1.1e-07	1.4e-06	2.3e-06	7.0e-06
3.85	1.1e-07	1.4e-06	2.4e-06	7.4e-06
3.96	1.0e-07	1.3e-06	2.2e-06	6.8e-06
4.07	1.0e-07	1.2e-06	2.2e-06	6.8e-06
4.18	8.9e-08	1.1e-06	2.0e-06	6.2e-06
4.29	8.6e-08	1.1e-06	1.9e-06	5.9e-06
4.40	7.9e-08	9.9e-07	1.7e-06	5.3e-06
4.51	6.8e-08	8.5e-07	1.5e-06	4.5e-06
4.62	6.1e-08	7.7e-07	1.4e-06	4.2e-06
4.73	5.3e-08	6.6e-07	1.2e-06	3.8e-06
4.84	5.0e-08	6.3e-07	1.2e-06	3.5e-06
4.95	4.7e-08	6.0e-07	1.1e-06	3.3e-06
5.06	4.5e-08	5.6e-07	1.1e-06	3.3e-06
5.17	4.5e-08	5.7e-07	1.2e-06	3.5e-06
5.28	4.5e-08	5.7e-07	1.2e-06	3.5e-06
5.39	4.6e-08	5.9e-07	1.3e-06	3.7e-06
5.50	4.3e-08	5.4e-07	1.1e-06	3.3e-06
5.61	4.6e-08	5.9e-07	1.2e-06	3.6e-06
5.72	4.7e-08	6.0e-07	1.2e-06	3.5e-06
5.83	4.5e-08	5.7e-07	1.1e-06	3.3e-06
5.94	4.5e-08	5.6e-07	1.0e-06	3.1e-06
6.05	3.9e-08	4.9e-07	8.5e-07	2.6e-06
6.16	3.9e-08	4.8e-07	8.1e-07	2.5e-06
6.27	3.6e-08	4.4e-07	7.4e-07	2.3e-06
6.38	3.3e-08	4.0e-07	6.6e-07	2.0e-06
6.49	3.1e-08	3.7e-07	6.0e-07	1.8e-06
6.60	2.9e-08	3.4e-07	5.5e-07	1.7e-06
6.71	2.7e-08	3.1e-07	5.0e-07	1.5e-06
6.82	2.6e-08	3.0e-07	4.9e-07	1.5e-06
6.93	2.4e-08	2.8e-07	4.6e-07	1.4e-06
7.04	2.3e-08	2.7e-07	4.4e-07	1.3e-06
7.15	2.2e-08	2.6e-07	4.1e-07	1.2e-06
7.26	2.0e-08	2.4e-07	3.7e-07	1.1e-06
7.37	1.9e-08	2.3e-07	3.5e-07	1.1e-06
7.48	1.7e-08	2.1e-07	3.2e-07	1.0e-06
7.59	1.9e-08	2.3e-07	3.4e-07	1.1e-06
7.70	1.6e-08	2.0e-07	2.9e-07	9.1e-07

Table 12. continued.

Ang.Dist.[″]	k_A	k_B	k_C	k_D
7.81	1.7e-08	2.1e-07	3.2e-07	9.8e-07
7.92	1.5e-08	1.8e-07	2.9e-07	8.9e-07
8.03	1.4e-08	1.8e-07	3.0e-07	9.2e-07
8.14	1.3e-08	1.6e-07	2.8e-07	8.6e-07
8.25	1.1e-08	1.4e-07	2.4e-07	7.5e-07
8.36	1.1e-08	1.4e-07	2.4e-07	7.5e-07
8.47	1.1e-08	1.3e-07	2.3e-07	7.1e-07
8.58	1.1e-08	1.3e-07	2.2e-07	6.8e-07
8.69	1.0e-08	1.2e-07	2.1e-07	6.4e-07
8.80	1.0e-08	1.2e-07	2.0e-07	6.2e-07
8.91	1.0e-08	1.2e-07	2.0e-07	6.2e-07
9.02	9.8e-09	1.2e-07	2.0e-07	6.1e-07
9.13	9.2e-09	1.1e-07	1.9e-07	5.9e-07
9.24	8.6e-09	1.0e-07	1.8e-07	5.6e-07
9.35	8.1e-09	9.9e-08	1.8e-07	5.5e-07
9.46	7.9e-09	9.7e-08	1.8e-07	5.4e-07
9.57	7.5e-09	9.0e-08	1.7e-07	5.3e-07
9.68	7.3e-09	8.8e-08	1.7e-07	5.1e-07
9.79	7.1e-09	8.5e-08	1.6e-07	4.8e-07
9.90	7.0e-09	8.5e-08	1.5e-07	4.7e-07
10.01	6.7e-09	8.1e-08	1.5e-07	4.6e-07
10.12	6.4e-09	7.6e-08	1.4e-07	4.4e-07
10.23	6.1e-09	7.3e-08	1.3e-07	4.1e-07
10.34	5.8e-09	6.9e-08	1.3e-07	3.9e-07
10.45	5.7e-09	6.9e-08	1.3e-07	3.8e-07
10.56	5.2e-09	6.2e-08	1.2e-07	3.5e-07
10.67	5.3e-09	6.4e-08	1.2e-07	3.7e-07
10.78	5.0e-09	5.9e-08	1.1e-07	3.4e-07
10.89	5.5e-09	6.6e-08	1.2e-07	3.6e-07
11.00	5.6e-09	6.7e-08	1.2e-07	3.7e-07